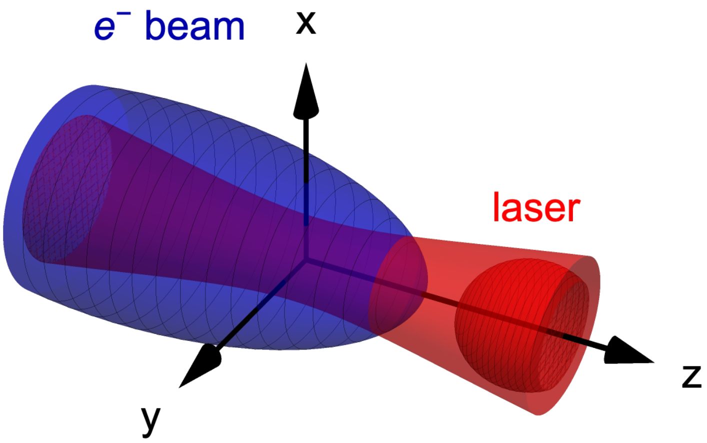

Classical and Quantum simulation of Extreme Plasma Physics

Óscar Löfgren Amaro

Thesis to obtain the Master of Science Degree in

Engineering Physics

Supervisor: Prof. Marija Vranic

Examination Committee

Chairperson: Prof. João Alberto dos Santos Mendanha Dias
Supervisor: Prof. Marija Vranic
Members of the Committee: Prof. Jorge Miguel Ramos Domingues Ferreira Vieira
Dr. Lorenzo Buffoni

December 2021

Acknowledgments

This work was supported in part through the Programme *New Talents in Quantum Technologies* of the Gulbenkian Foundation (Portugal) and through a studentship at GoLP-EPP. I acknowledge PRACE for awarding access to MareNostrum based in the Barcelona Supercomputing Centre, and GoLP-EPP for access to the Accelerates cluster.

In general, I would like to thank everyone at GoLP, who are exemplary researchers and people, and for *continuously raising the bar*.

I would like to thank my supervisor Dr. Marija Vranic for her continuous guidance, patience and strong sense of work ethics through all the years I have been at GoLP-EPP.

I would like to thank Dr. Bertrand Martinez for fruitful discussions and support with simulations.

I would like to thank Diogo Cruz for his patience to answer many of my questions on quantum algorithms, without which the path towards finishing this thesis would have been much more chaotic.

I would like to thank my colleagues and friends along these five years of MEFT, in particular Filipe, Tiago, Gonçalo and Nuno for their very interesting discussions, feedback and camaraderie throughout the development of this thesis.

Finally I would like to thank my parents for their support during all these years.

Resumo

Os avanços recentes em tecnologia de lasers vão em breve permitir explorar novos regimes da electrodinâmica. Uma das experiências mais promissoras para a observação de sinais de Electrodinâmica Quântica é a colisão frontal entre electrões relativistas e um impulso laser ultra-intenso.

Geralmente para se estimar com precisão os observáveis nestas experiências é preciso recorrer a simulações de primeiros princípios (como códigos partícula-em-célula com rotinas de Monte Carlo), que são computacionalmente dispendiosas. Além disso, os modelos analíticos existentes restringem-se habitualmente a cenários altamente idealizados como no caso de uma onda plana, que não se transferem bem para experiências.

Neste trabalho propomos uma nova abordagem semi-analítica para cenários de colisão realistas, que permite generalizar leis de escala originalmente derivadas para uma onda plana. Este método permite estimar com precisão e optimizar o número de positrões ao variar a focagem do laser.

Numa linha paralela de trabalho, investigamos o potencial uso de Computação Quântica (CQ) para modelar plasmas extremos. Este novo paradigma de processamento de informação promete acelerar os cálculos em certas classes de problemas nas próximas décadas. Apesar de estar já bem desenvolvida nas áreas adjacentes à Mecânica Quântica, a CQ está ainda na sua infância no que diz respeito à Física de Plasmas. Nós destacamos alguns cenários onde novos algoritmos quânticos poderiam ser desenvolvidos.

Palavras-chave: Física de Plasmas; Reação da Radiação; Electrodinâmica Quântica; Simulações Partícula-em-Célula; Computação Quântica; Computação de Alta Performance;

Abstract

Recent advances in laser technology will soon allow explorations into new regimes of electrodynamics. One of the most promising experiments to observe signals from Strong-field Quantum Electrodynamics is head-on collision between an energetic electron beam and an ultra-intense laser pulse.

Accurate estimates of observables in these experiments usually require *ab-initio* simulations (e.g., Particle-in-cell codes with Monte Carlo routines), which are computationally expensive. Furthermore, analytical models usually restrict to highly idealized setups, like the plane wave, which do not map well to experiments.

In this work, we propose a new semi-analytical approach to focused beam-laser scattering, which allows extending scaling laws originally derived for plane wave to realistic scenarios. This method leads to accurate estimation and optimization of the positron yield by changing the laser spotsize.

In a parallel line of work, we investigate the potential use of Quantum Computing (QC) to model extreme plasmas. This new information processing paradigm promises significant speedups for certain classes of problems in the coming decades. Although already somewhat mature in the areas adjacent to Quantum Mechanics, QC is still in its cradle regarding Plasma Physics. We highlight several scenarios where new quantum algorithms could be developed.

Keywords: Plasma Physics; Radiation reaction; Quantum Electrodynamics; PIC simulations; Quantum Computing; High Performance Computing;

Contents

Acknowledgments . . . iii

Resumo . . . v

Abstract . . . vii

List of Tables . . . x

List of Figures . . . xi

Nomenclature . . . xiv

Acronyms . . . xv

1 Introduction 1

1.1 Motivation . . . 1

1.2 Objectives . . . 5

1.3 Outline . . . 5

1.4 Original contributions . . . 5

2 The Particle-in-cell method 8

2.1 The PIC loop . . . 8

2.2 Simulating QED phenomena . . . 9

3 Particle distributions according to the effective laser intensity they interact with 13

3.1 Positron production in a Plane Wave . . . 13

3.2 Beyond Plane Wave . . . 14

3.3 Short beam . . . 17

3.4 Thin beam . . . 18

3.5 Wide beam . . . 19

3.5.1 Alternative derivation of the particle distribution . . . 20

3.6 Detailed particle distribution functions in centered and non-centered laser collisions . . . 21

3.7 Observations . . . 23

3.8 Conclusions . . . 24

4 Optimal focusing strategy to obtain the maximum positron yield 27

4.1 Introduction . . . 27

4.2 Varying the laser spotsize . . . 27

4.3 Parameter study for future laser facilities 28
4.4 Effect of longitudinal jitter 28
4.5 Conclusions 30

5 Basics of Quantum Computing **31**
5.1 Introduction 31
5.2 Entanglement 32
5.3 Bloch sphere 32
5.4 Frequently used gates 33

6 Applications of Quantum Computing **35**
6.1 Introduction 35
6.2 Building blocks 35
    6.2.1 Standard Hamiltonian 35
    6.2.2 Linear Schrödinger equation 36
6.3 Linear dynamics 37
    6.3.1 Linear Vlasov 37
    6.3.2 Fokker-Planck equation 38
    6.3.3 Plasma-QED Kinetic equations 39
6.4 Carleman linearization 40
    6.4.1 Introduction 40
    6.4.2 Applying Carleman linearization to Kompaneets equation 40
6.5 Variational Quantum Algorithms 41
    6.5.1 Introduction 41
    6.5.2 The SWAP algorithm 42
    6.5.3 Simulating cubic gates 43
6.6 Conclusions 44

7 Conclusions **45**
7.1 Achievements 45
7.2 Code Contributions 45
7.3 Open Questions and Future Work 46

Bibliography **47**

List of Tables

3.1 Particle distributions according to the effective vector potential for different beam geometries. Here, $a_z \equiv a_0/\sqrt{1+(L/4z_R)^2}$ is the $a_{0,\text{eff}}$ associated with the integration limits imposed by the longitudinal size of the electron beam, N_b represents the total number of particles in the beam, n_b is the beam density, R and L are the beam radius and length respectively. The laser spot size is W_0, $z_R \equiv \pi W_0^2/\lambda$ is the Rayleigh length, $\Delta_\perp$ is the perpendicular displacement of the beam centre from the laser propagation axis, and I_0 is a Bessel function of the first kind. 22

3.2 Particle distributions for arbitrary temporal synchronization. The ± sign corresponds to situations where $\Delta_\| < L/4$ or $\Delta_\| > L/4$ respectively, and $z_\pm = \Delta_\| \pm L/4$. $\theta(x)$ is the Heaviside Theta function, $a_{z_\pm} = a_0/\sqrt{1+(z_\pm/z_R)^2}$ and $a_\| = a_0/\sqrt{1+(\Delta_\|/z_R)^2}$. 23

5.1 List of frequently used quantum gates. 34

List of Figures

1.1 Evolution of peak laser intensity since its invention and the regimes each intensity allows to study. Figure from [43]. 2

1.2 Scattering of a relativistic electron beam (blue) and a counter-propagating laser pulse (red). 4

2.1 Particle-in-cell simulation grid. Field values are saved in the grid corners, while particles are free to move within and between grid cells, subject to the effects of the fields. 8

2.2 PIC-QED loop for one time step. Particles are labeled p and the grid indexes are i. 9

2.3 Feynman diagrams of the dominant QED processes in this thesis. a) Nonlinear Compton Scattering b) Breit-Wheeler Pair Production. 10

2.4 Dominant QED processes in this thesis. Left: Nonlinear Compton Scattering. Right: Breit-Wheeler Pair Production. The differential rates were normalized such that the area under the curves is unity. 10

3.1 A volume element between two isosurfaces of the effective normalized vector potential $a_{0,\text{eff}}$. The volume element contains all the points where particles experience the peak a_0 within the interval $[a_{0,\text{eff}}, a_{0,\text{eff}} + \mathrm{d}a_{0,\text{eff}}]$. 15

3.2 Scattering with nontrivial electron beam shapes. a) A single electron-laser interaction equivalent to electron colliding with a plane wave packet ($L \ll z_R,\ R \ll W_0$). b) Interaction with a wide electron beam ($R \gg W_0$). c) Interaction with a pencil-like thin electron beam ($R \ll W_0$). d) Interaction with a short electron beam ($L \ll z_R$). 17

3.3 Short beam. a) Particle distribution according to the effective vector potential for a transversely aligned beam ($\Delta_\perp = 0$). b) Positron yield as a function of transverse beam displacement from the laser propagation axis $\Delta_\perp$. The electron beam energy is $E_0 = 2\ \text{GeV}$, charge is $Q_b = 100\ \text{pC}$ and Gaussian radius $R = 6\ \mu\text{m}$ in all spatial directions. The laser parameters are $a_0 = 48.4, \lambda = 0.8\ \mu\text{m}, \tau = 30\ \text{fs}$ and $W_0 =\ 2\mu\text{m}$. 18

3.4 Thin beam. a) Particle distribution according to the effective vector potential for $\Delta_\parallel = 0$. b) Positron yield as a function of temporal synchronization. The beam energy is $E_0 = 13\ \text{GeV}$, charge is $Q_b =\ 1\ \text{pC}$ and length $L = 200\ \mu\text{m}$. The laser parameters are $a_0 = 48.4,\ \lambda = 0.8\ \mu\text{m},\ \tau = 35\ \text{fs},\ W_0 = 3\ \mu\text{m}$ and $\Delta_\parallel$ represents the longitudinal displacement of the beam centre when the laser is at the focus. 18

3.5 Wide beam. a) Particle distribution according to the effective laser vector potential $a_{0,\text{eff}}$. Dashed lines are analytical expressions, circles are from sampling and full line corresponds to the limiting case of $L \to \infty$. b) Positron yield as a function of the longitudinal displacement $\Delta_{\|}$ for one beamlet. The laser parameters are $a_0 = 7.3$, $\lambda = 0.8\ \mu\text{m}$, $\tau = 31$ fs and $W_0 = 3\ \mu\text{m}$. The beam energy is $E_0 = 13$ GeV, transverse width $\sigma_x = 24.4\ \mu\text{m}$ and $\sigma_y =\ 29.6\ \mu\text{m}$. The beam length is $L = 50.9\ \mu\text{m}$ for each beamlet, while the entire beam contains $Q = 2$ nC and is $250\ \mu\text{m}$-long. 20

3.6 a) A partially synchronized electron beam. b) Electron beam with a large temporal offset. The beam represented in grey can be expressed as a linear combination of the beams represented in blue and yellow. 23

4.1 a) Positron yield as a function of the laser spot size keeping the total energy contained within the laser pulse constant at $\varepsilon = 1$ kJ. b) Optimal spot size for different total laser pulse energies. Beam parameters are $E_0 = 10\ \text{GeV}, L = 200\ \mu\text{m}, \sigma_x = 24.4\ \mu\text{m}, \sigma_y = 29.6\ \mu\text{m}, n_b = 10^{16}\ \text{cm}^{-3}$, and we consider $\tau = 150$ fs with $\lambda = 0.8\ \mu\text{m}$. 28

4.2 Optimization study for lasers pulses of fixed duration ($\tau = 35$ fs). a) Optimal laser spotsize for a head-on scattering as a function of total pulse energy and the electron energy. b) Positron yield achieved using the optimal spotsize. The laser wavelength is $\lambda = 0.8\ \mu\text{m}$; the electron beam is $L = 200\ \mu\text{m}$ long (flat-top longitudinal profile) 29

4.3 Optimization study for fixed electron beam parameters (here, electron energy is 13 GeV, corresponding to an accelerator beam available for example at SLAC). a) Optimal laser spotsize for a head-on scattering as a function of pulse energy and duration. b) Positron yield achieved using the optimal spotsize. Other laser and electron parameters are the same as in figure 4.2 29

4.4 Effect of longitudinal jitter of laser on the positron yield. Beam parameters are $E_0 = 3\ \text{GeV}, L = 10\ \mu\text{m}$ and laser parameters $\tau = 30.92\ \text{fs}, \lambda = 0.8\ \mu\text{m}, W_0 = 3\ \mu\text{m}$. The gray area indicates the region for intermediate values of jitter. 29

5.1 Geometrical representation of the state $|\psi\rangle$ of a single qubit using the Bloch sphere. . . . 33

6.1 Simulation of the Hamiltonian $H = Z^{\otimes 3}$ for an interval Δt. 36

6.2 Evolution of $|\psi|^2$ for a wavepacket in an harmonic potential. 37

6.3 Matrix representation of the evolution operator in equation 6.13. 40

6.4 Solution of the nonlinear Kompaneets equation using the Carleman linearization technique up to order $N = 2$. 41

6.5 Schematic of a variational circuit for dynamical evolution using the original SWAP test. $\vec{\theta}$ and $\vec{\theta}'$ represent the parameters at time t and $t + \Delta t$, respectively. 42

6.6 Left: schematic of the BBA circuit by Cincio *et al* [98] to measure the overlap between states ρ and σ. Right: simulation results of from a IBM machine *ibmq_manila*. 43

6.7 Left: compiled circuit. Middle: associated error. Right: Non-compiled circuit. The $|\alpha_i|^2$ correspond to the probabilities of measuring the system in state $|\alpha_i\rangle$. 43

6.8 Ideal simulation of a variational circuit for the three-wave mixing. a) Circuit of a 1-block ansatz. b) Variational evolution of the $|\alpha_2|^2$ observable with a 1-block ansatz. c) Circuit of a 2-block ansatz and d) respective evolution. 44

Nomenclature

Greek symbols

$\sigma_x, \sigma_y, \sigma_z$	Pauli operators.

Roman symbols

I	Identity operator.
X, Y, Z	Pauli operators.

Subscripts

x, y, z	Cartesian coordinates.

Superscripts

†	Conjugate transpose.
T	Transpose.

Acronyms

ELI Extreme Light Infrastructure.

EPP Extreme Plasma Physics.

GoLP Group of Lasers and Plasmas.

HHL Harrow-Hassidim-Lloyd algorithm.

IST Instituto Superior Técnico.

LAD Lorentz-Abraham-Dirac equation.

LHS Left Hand Side.

LL Landau-Lifschitz equation.

LWFA Laser WakeField Acceleration.

NISQ Noisy Intermediate-Scale Quantum.

PIC Particle-in-Cell.

QC Quantum Computing.

QED Quantum Electrodynamics.

QFT Quantum Fourier Transform.

RHS Right Hand Side.

VQE Variational Quantum Eigensolver.

Chapter 1

Introduction

1.1 Motivation

Plasma Physics is the field of many-body long-range electromagnetic interactions. A plasma is a state of matter in which charged particles are mostly free (few bound atoms or molecules) and collective phenomena dominate (as opposed to interparticle collisions), and is the most abundant form of ordinary matter in the universe.

Plasmas permeate most of the visible universe and are fundamental to understand fusion in stars, turbulence, and the origin of magnetic fields in space. Recent progress in laser technology and particle acceleration will allow for experiments in ultrarelativistic and quantum electrodynamical processes in plasmas to be performed [1]. At the same time, the dynamics of astrophysical objects such as pulsar magnetospheres and polar caps [2–4], and jets from and accretion disks around black holes [5, 6] depend heavily on Plasma Physics.

In an intense electromagnetic background, charged particles obtain relativistic velocities and emit energetic photons. A fraction of these photons decays into electron-positron pairs, which can themselves be accelerated by the fields and radiate new photons [7, 8]. Although Quantum Electrodynamics (QED) is one of the most thoroughly verified physical theories for elementary processes, the rich dynamics arising from plasmas' collective behavior is still poorly understood. The repeated recurrence of photon emission and pair creation can lead to the formation of the so-called QED cascades, where the number of particles in a plasma grows exponentially with time. Other quantum effects include: quantum vacuum polarization, light-by-light scattering, vacuum birefringence, four-wave mixing, and high order harmonic generation from the vacuum [9–16].

These phenomena are part of the subfield of Extreme Plasma Physics, which depends on heavy numerical computations due to its inherent nonlinearity. Simulations are crucial to understanding the spatiotemporal structure of the electromagnetic fields, as they are not known in advance. In particular, these fields can be depleted during the interaction with the plasma, as energy is transferred to particles and radiation, invalidating analytical calculations that assume an external field structure. It would, therefore, greatly benefit from new algorithm development, namely in the quantum paradigm.

It was recently proposed that one could re-create in the laboratory an energy density comparable to those of extreme astrophysical scenarios using counter-propagating intense laser pulses [1], which has prompted many scientists to study related configurations using kinetic particle-in-cell simulations [17–37]. However, as the required laser intensity $I \sim 10^{24}\ \mathrm{W/cm^2}$ is still beyond the extent of the current laser technology (the record is $I \sim 10^{23}\ \mathrm{W/cm^2}$ [38]), there are many unknowns about the highly nonlinear dynamics associated with plasmas in these extreme conditions. Before lasers become sufficiently intense to generate dense e^+e^- pair plasmas from light alone, a head-on collision between a pulsed laser and a very energetic electron beam can produce dilute e^+e^- beams by applying currently available technology [39]. Even when energetic electron beams are not available in a given facility, previous proposals [40, 41] have suggested that the required laser intensity for copious GeV pair production in near-critical-density plasmas can be reduced to the order of $I \sim 10^{22}\ \mathrm{W/cm^2}$, thereby allowing the study of some of these extreme phenomena in more conventional laser systems.

Most of present-day high-power lasers build upon the technique of Chirped Pulse Amplification (CPA), which amplifies a ultrashort laser pulse to the petawatt level. In simplified terms, the laser pulse is stretched out temporally and spectrally, then amplified, and then compressed again. This method was introduced in the context of optical lasers by Donna Strickland and Gérard Mourou in the mid-1980s at the University of Rochester [42], work for which they were awarded the Nobel Prize in Physics in 2018. This technology lead to an exponential rise in peak intensity shortly after its invention (see figure 1.1).

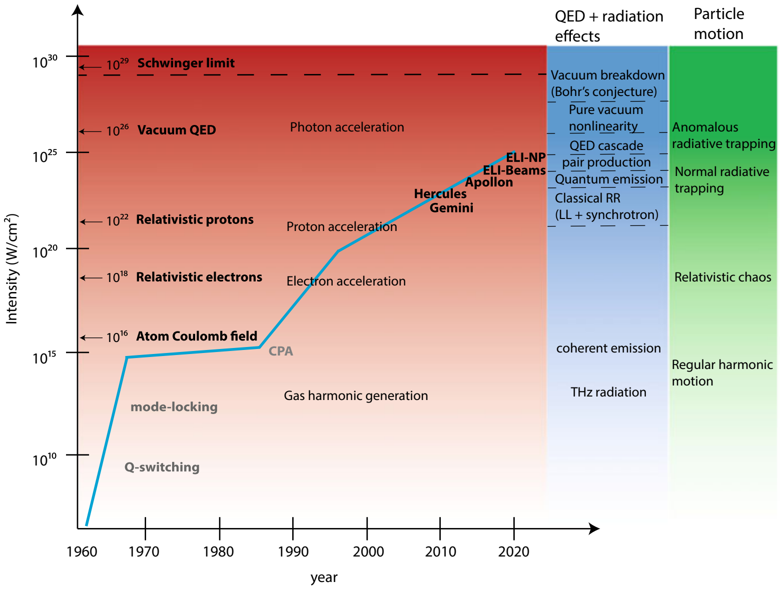

Figure 1.1: Evolution of peak laser intensity since its invention and the regimes each intensity allows to study. Figure from [43].

The fact that plasma is already “a destroyed material” (the atomic bonds are broken, which means the electrons and ions are free charges) allows sustaining much higher electromagnetic fields than conventional accelerators. The technique of Laser Wakefield Acceleration (LWFA) [44] consists of sending a laser pulse through a plasma and using the EM wake generated to accelerate electrons in very short distances. This allows having energetic beams and intense lasers in the same laboratory, which enables the study of electron-laser scattering. Currently, conventional accelerators still allow for better quality and control than LWFA because its technology is more mature. However, as LWFA becomes a standard scientific tool, laboratories can become increasingly more compact and use a single laser system for acceleration and scattering.

Research on stochastic effects in radiation reaction is also expected to benefit from the laser-electron scattering experiments [45–49], with new ways to infer the peak laser intensity at collision [50, 51] and probing the transition from the classical to the quantum-dominated laser-electron interaction. Two all-optical experiments have shown the electron slowdown due to radiation reaction [52, 53], but were not able to discriminate between different theoretical descriptions of radiation reaction. We anticipate the near-future facilities (e.g. ELI [54], Apollon [55], CoReLS [56], FACET-II [57, 58], LUXE [59], EXCELS [60], ZEUS[61]) to probe the electron-positron pair production covering several different regimes of interaction.

This Thesis focuses on head-on laser-electron scattering (see figure 1.2) that maximizes the strength of the electric field in the electron rest frame in comparison with other scattering angles. This is the first experiment planned in most of the aforementioned facilities, and we aim to improve the current predictive capabilities for positron creation.

Due to the inherent non-linearity of the Breit-Wheeler pair production, there is no general roadmap on what would be an optimal strategy to obtain the highest possible positron yield using any given laser system. If the laser is assumed to be a plane wave (adequate when the laser is much wider than the interacting beam), the analytical predictions state that the best strategy would be to use the highest conceivable laser intensity. Therefore it is tempting to conclude that the laser should be focused on the smallest attainable focal spot. Our work shows that this strategy may not always be optimal, as there is a trade-off between the high laser intensity and the size of the scattering volume. With a short focus, the highest intensity region becomes small both transversely and longitudinally, which can reduce the number of seed electrons that interact with the close-to-the-maximum intensity, as well as the duration of this collision.

Each of the mentioned factors affects the resulting number of positrons; hence a correct optimization strategy would have to take all of them into account at the same time. This can be achieved by resorting to full-scale 3-dimensional particle-in-cell simulations, making sure enough statistics is used to represent the interacting electron beam with all its features, as well as high grid resolution in all spatial directions to correctly describe the laser dynamics. This approach requires a lot of computational resources (several million CPU-hours for each parameter set) and can be justified for the support of a specific ongoing experiment where most parameters are not free. However, for future experiments, there are many possible parameter choices. It would thus be practical to devise a simple and cost-effective way for their consideration. This would ensure that the best possible strategies are applied when constructing new laser facilities. The first part of this thesis is focused towards helping achieve that goal.

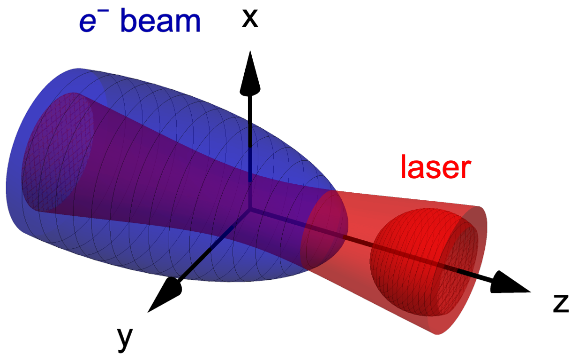

Figure 1.2: Scattering of a relativistic electron beam (blue) and a counter-propagating laser pulse (red).

The second part is dedicated to Quantum Computing, which is a new computing paradigm. It relies on the laws of quantum mechanics to process information in a non-classical manner and may offer advantages over standard techniques in some situations.

The idea of quantum computation, as suggested by Feynman [62], Manin and others, was primarily motivated by the problem of quantum simulation. There are already quantum machines capable of simulating small molecules and other systems, which may accelerate progress in fundamental Science and industrial applications. Recently [63], a collaboration between Google, NASA and Oak Ridge National Laboratory demonstrated the ability of a 53-qubit quantum processor to perform in seconds what would take the largest classical supercomputers today thousands of years, contributing to narrow the gap between these two very different paradigms of computation.

We are now in the so-called Noisy Intermediate-Scale Quantum, or NISQ era [64], in which quantum hardware still faces many issues on performance, limiting the number of qubits (< 100) and the number of quantum operations (< 100) allowed in a single computation. Until error-corrected codes and better hardware are developed, algorithms need to be designed considering these constraints.

The development of quantum algorithms in Physics has been mainly motivated by fundamental Quantum Mechanics, Quantum Chemistry, and Condensed Matter problems. Only recently has there been an interest in developing quantum versions of algorithms used in Plasma Physics, leveraging the extensive know-how of this scientific community [65]. This late development of the field is partly justified by the inherent difficulty of solving nonlinear problems in quantum computers and the recent progress on quantum hardware.

In recent years, some quantum techniques have been suggested to solve nonlinear problems [66–69]. However, these algorithms are usually non-trivial to implement, as they require a solid technical background, and a general quantum computing approach for problems in plasma physics is still lacking. Current algorithms typically limit themselves to highly idealized setups of one dimension or simple electromagnetic field configurations.

1.2 Objectives

The first part of this Thesis focuses on extending the scaling laws for pair production in laser-electron scattering, previously derived in a plane wave approximation, to diffraction-limited Gaussian laser pulses and finite electron beams. The main objective is to be able to describe realistic experimental configurations, where spatio-temporal synchronisation of the interaction depends on many factors, and this can affect the total yield of electron-positron pairs obtained. Our method allows predicting the number of positrons created in a laser-electron collision with a temporal (longitudinal) or a perpendicular offset. With the analytical model proposed in this Thesis, predictions can be obtained without resorting to expensive massively-parallel simulations. The most demanding calculation required is a numerical integration of an analytical function that can be performed on a single CPU, and the results obtained within minutes. These results are benchmarked with full-scale 3-dimensional particle-in-cell simulations from the code `OSIRIS` [70]. This aims to simplify the pair production optimization in a multi-variable parameter space. Even though we focus here on pair production, the main ideas of this work can be applied to other observables in focused laser scattering experiments.

In the second part, we aim to develop new algorithms for the simulation of extreme plasmas. We use the codes Qiskit [71] and PennyLane [72] to implement several quantum algorithms. We evaluate current solutions and comment on the best path towards their generalizations.

1.3 Outline

This thesis is structured as follows. In Chapter 2, we introduce the basics of the Particle-in-cell method and how quantum electrodynamical effects are included in simulations. In Chapter 3, we introduce the scaling law for positron production in a Plane Wave and we derive the analytical distribution of particles in $a_{0,\mathrm{eff}}$ for a general setup, introduce the alternative sampling approach, apply both to three different beam geometries, and calculate the total number of positrons in each. In Chapter 4 we address the issue of optimization of the positron yield for varying spotsize and compute expected values for near-future laser facilities. In Chapter 5 we review the basics of Quantum Computing, while in Chapter 6 we discuss possible applications of quantum algorithms to model extreme plasma physics.

1.4 Original contributions

The main original contribution of this Thesis are the development of particle distributions in effective a_0, which could help design future experiments in laser-electron or laser-photon scattering, and the identification of scenarios within extreme plasma physics where quantum algorithms could be developed. The work presented in this Thesis led to the following scientific communications and publications:

Papers

- Ó. Amaro, M. Vranic, *Optimal laser focusing for positron production in laser-electron scattering* [73] [1]: Amaro et al 2021 New J. Phys. `https://doi.org/10.1088/1367-2630/ac2e83`, pre-print `https://arxiv.org/abs/2106.01877`

Presentations at international meetings

- Ó. Amaro, M. Vranic, *Optimal laser focusing for positron production in laser-electron scattering* [1], Laser-Plasma Summer School (LAPLASS) 2020, September 2020, `https://www.clpu.es/LAPLASS2020`

- Ó. Amaro, M. Vranic, *Optimal laser focusing for positron production in laser-electron scattering* [1], American Physical Society - Division of Plasma Physics 62nd Annual Meeting, November 2020, `https://meetings.aps.org/Meeting/DPP20/Session/JP13.100`

- Ó. Amaro, M. Vranic, *Maximizing positron production in laser-electron scattering* [1], European Physical Society Conference on Plasma Physics 2020, June 2021

- Ó. Amaro, M. Vranic, *Simulating extreme plasma physics on a quantum computer* [2], European Physical Society Conference on Plasma Physics 2020 HIFI-LASA, June 2021

- Ó. Amaro, M. Vranic, *Laser focusing strategies for positron production in laser-electron scattering* [1], ELI Summer School 2021, August 2021, `https://indico.eli-beams.eu/event/393/page/347-welcome`

- Ó. Amaro, M. Vranic, *Effects of electron beam geometry in the production of pairs in laser-electron scattering* [1], ExHILP 2021, September 2021, `https://indico.tpi.uni-jena.de/event/194/overview`

Presentations at national meetings

- Ó. Amaro, M. Vranic, *Focagem óptima para a produção de pares em colisões laser-feixe de eletrões* [1], Sociedade Portuguesa de Física (SPF) Física2020, September 2020, `https://fisica2020.spf.pt/index`

- Ó. Amaro, M. Vranic, *Optimal laser focusing for positron production in laser electron scattering* [1], Jornadas de Engenharia Física (IST) 2021, March 2021

- Ó. Amaro, M. Vranic, *Towards quantum simulation of extreme plasmas* [2], Quantum for Plasma Plasma for Quantum (QPPQ) Seminar, July 2021 `http://epp.ist.utl.pt/qppq/`

Collaborations

- Collaboration with the CoReLS group, where the $a_{0,\text{eff}}$ approach was applied to estimate the average photon energy and total number of photons produced in the electron-laser scattering and compare with experimental results [1], `https://corels.ibs.re.kr/html/corels_en/`.

- Collaboration with other GoLP-EPP members, with the goal of better estimating the number of positrons produced in a photon-laser scattering at 90º, through the $a_{0,\text{eff}}$ approach developed in this Thesis [1].

Awards

- Best Pecha Kucha (fast-paced 10 minute presentation) at the LAPLASS 2020 Summer School, awarded by Laserlab-Europe
- Best poster in the Plasma Physics category at the Física 2020 conference, awarded by Sociedade Portuguesa de Física
- Best undergraduate poster at American Physical Society - Division of Plasma Physics 2020, awarded by the APS-DPP
- Best poster at Jornadas de Engenharia Física, Instituto Superior Técnico, 2021
- New Talents in Quantum Technologies studentship 2020-2021, awarded by the Gulbenkian Foundation

[1] - Referring to work on Optimal Focusing for Positron Production

[2] - Referring to work on Quantum Algorithms

Chapter 2

The Particle-in-cell method

2.1 The PIC loop

There are several possible descriptions of a plasma, each having its own characteristic length and time scales. In numerical laser-plasma kinetics, the most accurate approach is the Particle-in-cell approach (PIC), which solves the relativistic Klimontovich equation on a computer

$$\frac{\partial}{\partial t} f_\alpha + \mathbf{v} \cdot \frac{\partial}{\partial \mathbf{x}} f_\alpha + q_\alpha (\mathbf{E} + \mathbf{v} \times \mathbf{B}) \cdot \frac{\partial}{\partial \mathbf{p}} f_\alpha = 0 \tag{2.1}$$

where $f_\alpha(\mathbf{x}, \mathbf{p}, t)$ represents the density of particles in phase space for each plasma species α, and $\mathbf{p} = \gamma\, m_\alpha \mathbf{v}$. The evolution of charged particles generates perturbations in the electromagnetic fields which are consistently coupled to Maxwell's equations

$$\begin{aligned} \nabla \cdot \mathbf{E} &= 4\pi\rho & \nabla \cdot \mathbf{B} &= 0 \\ \frac{\partial \mathbf{B}}{\partial t} &= -c\nabla \times \mathbf{E} & \frac{\partial \mathbf{E}}{\partial t} &= c\nabla \times \mathbf{B} - 4\pi \mathbf{j} \end{aligned} \tag{2.2}$$

In a PIC code, beam and plasmas are represented in a Lagrangian frame, while electromagnetic fields follow an Eulerian description, that is, only their value on a grid is stored (see figure 2.1). This reduces the code's complexity from $O(N^2)$ (if fields were to be computed for each pair of particles) to $\sim O(N)$ (the number of particles).

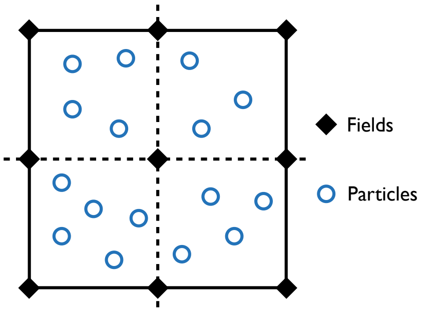

Figure 2.1: Particle-in-cell simulation grid. Field values are saved in the grid corners, while particles are free to move within and between grid cells, subject to the effects of the fields.

Even so, the PIC method can be computationally demanding when modeling large problems, for which most high-performance codes (e.g. `OSIRIS` [70]) resort to distributed computing. This approach consists of dividing the simulation domain into sub-regions assigned to different CPUs, each processing unit executing the code and communicating back the results to the other CPUs so that the system is evolved as a whole.

PIC codes execute a cycle of four steps at each time iteration (see figure 2.2): 1. evolution of the EM fields from the currents on the grid, 2. interpolation of field values to particle positions, 3. one time step particle push (usually following the Lorentz equation), and 4. deposition of current. This self-consistent loop evolves the coupled system of particles and fields efficiently and accurately. Besides this, it allows for the use of macroparticles, a coarse-grained version of a full particle description where an ensemble of particles shares their properties in phase-space. In these codes, the energy is conserved and transferred from the EM field to particles and vice versa.

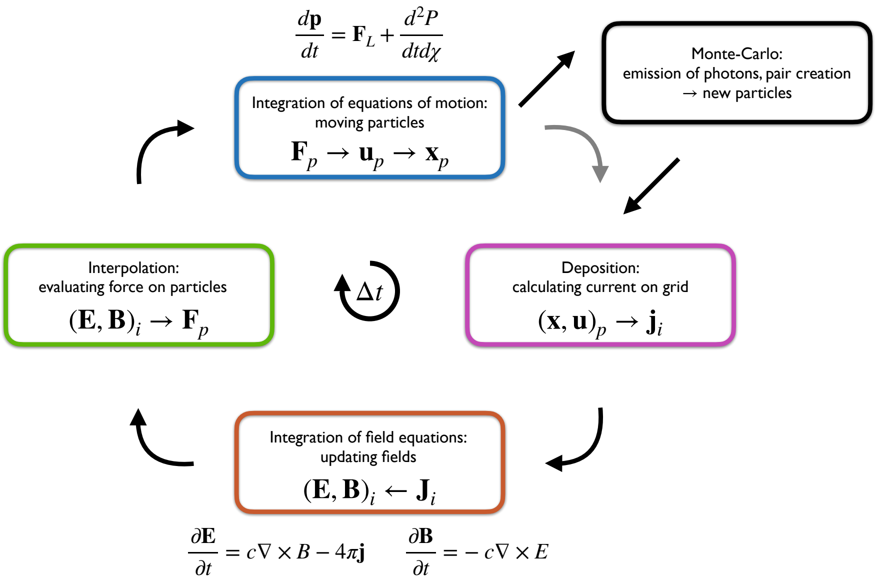
$\frac{d\mathbf{p}}{dt} = \mathbf{F}_L + \frac{d^2P}{dtd\chi}$
Integration of equations of motion: moving particles
$\mathbf{F}_p \to \mathbf{u}_p \to \mathbf{x}_p$
Monte-Carlo: emission of photons, pair creation → new particles
Interpolation: evaluating force on particles
$(\mathbf{E}, \mathbf{B})_i \to \mathbf{F}_p$
Δt
Deposition: calculating current on grid
$(\mathbf{x}, \mathbf{u})_p \to \mathbf{j}_i$
Integration of field equations: updating fields
$(\mathbf{E}, \mathbf{B})_i \leftarrow \mathbf{J}_i$
$\frac{\partial \mathbf{E}}{\partial t} = c\nabla \times B - 4\pi\mathbf{j}$
$\frac{\partial \mathbf{B}}{\partial t} = -c\nabla \times E$

Figure 2.2: PIC-QED loop for one time step. Particles are labeled p and the grid indexes are i.

In addition to the main PIC loop, a Monte Carlo module can be called to simulate production/decay of particles, which will be explained next.

2.2 Simulating QED phenomena

The dominant QED processes in the regimes explored in this Thesis are Nonlinear Compton Scattering and Breit-Wheeler Pair Production (see figure 2.3).

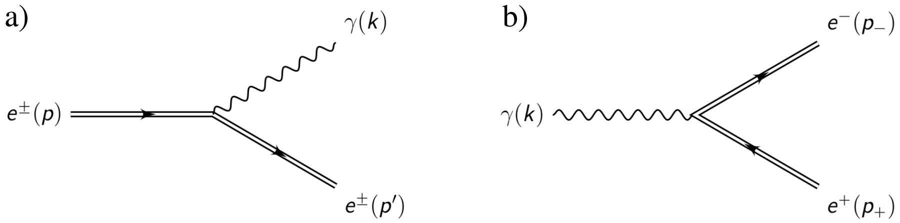

Figure 2.3: Feynman diagrams of the dominant QED processes in this thesis. a) Nonlinear Compton Scattering b) Breit-Wheeler Pair Production.

The probability distribution for the emission of a photon χ_γ by a lepton with χ_e follows [19]

$$\frac{\mathrm{d}^2P}{\mathrm{d}t\ \mathrm{d}\chi_\gamma} = \frac{\alpha mc^2}{\sqrt{3}\pi\hbar\gamma\chi_e}\left[\left(1-\xi+\frac{1}{1-\xi}\right)K_{2/3}(\tilde{\chi}) - \int_{\tilde{\chi}}^{\infty} K_{1/3}(x)\mathrm{d}x\right] \tag{2.3}$$

where $\tilde{\chi} = 2\xi/\left(3\chi_e(1-\xi)\right), \xi = \chi_\gamma/\chi_e$, m is the electron mass, α is the fine-structure constant, $\hbar$ the Planck constant, c speed of light in vacuum, and χ is a Lorentz invariant. The total probability of photon emission is the integral $\int \mathrm{d}^2P/\ \mathrm{d}t\ \mathrm{d}\chi_\gamma\ \mathrm{d}\chi_\gamma$. This quantity is calculated every time-step and compared to a pseudo-random number [28]. If the event is said to occur, the energy of the photon is sampled from the spectrum 2.3, the photon is introduced in the simulation and the lepton's energy is updated.

For Breit–Wheeler pair production, the algorithm is similar, but instead of emission, the photon decay's probabilities into an electron–positron pair are evaluated. If the event takes place, the photon is removed from the simulation, and the pair of new particles is initialised. Photons (real and virtual) can decay into electron-positron pairs in the presence of extreme fields according to

$$\frac{\mathrm{d}^2P}{\mathrm{d}t\ \mathrm{d}\chi_e} = \frac{\alpha m^2c^4}{\sqrt{3}\pi\hbar\omega\chi_\gamma}\left[\left(\frac{\xi^+}{\xi^-}+\frac{\xi^-}{\xi^+}\right)K_{2/3}(\tilde{\chi}) + \int_{\tilde{\chi}}^{\infty} K_{1/3}(x)\mathrm{d}x\right] \tag{2.4}$$

where $\tilde{\chi} = 2/\left(3\chi_\gamma\xi^+\xi^-\right)$, $\xi^+ = \chi_e/\chi_\gamma = 1-\xi^-$, and ω is the photon frequency.

These rates are shown in figure 2.4. In the case of Nonlinear Compton Scattering, in the regime $\chi_e \sim 0.1$ most photons emitted have much lower energies than the parent lepton, while for $\chi_e \gg 1$ photons with energies close to the lepton's start to become more probable.

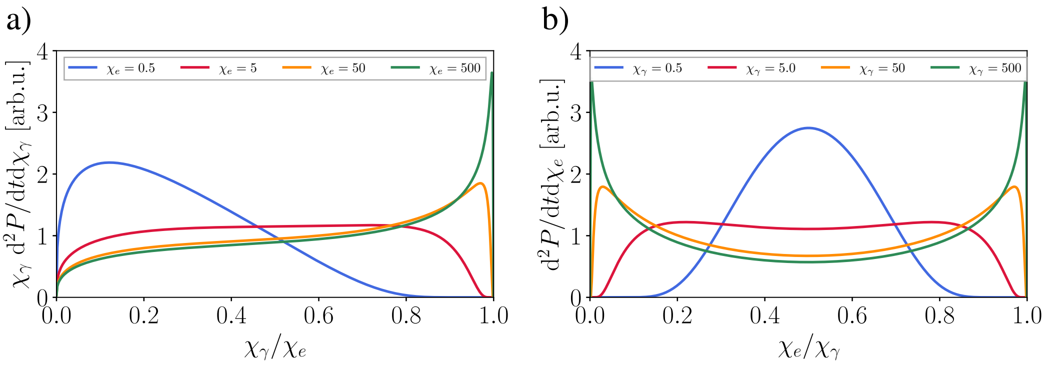

Figure 2.4: Dominant QED processes in this thesis. Left: Nonlinear Compton Scattering. Right: Breit-Wheeler Pair Production. The differential rates were normalized such that the area under the curves is unity.

When charged particles accelerate due to the action of fields, they emit radiation. To account for this effect, many PIC codes apply the Landau-Lifschitz equation [74], which has been recognized as the best description of classical radiation reaction.

While the particle's acceleration is small, the corrections to the trajectories due to radiation's recoil will remain a small perturbation. The magnitude of the radiation losses is quantified by the invariant classical radiation reaction parameter R_{c} [75]. Radiation damping becomes significant when $R_c > 0.01$ and dominates when $R_c > 0.1$.

From QED theory, we get an important quantity $E_{\mathrm{cr}} = 1.326 \times 10^{18}\ \mathrm{Vm}^{-1}$ which gives the threshold for which the vacuum becomes unstable for pair creation. It does work equal to the electron rest energy mc^2 over the Compton length $\lambda \equiv \hbar/mc$. The equivalent magnetic field strength is $B_{\mathrm{Sch}} \equiv E_{\mathrm{Sch}}/c = 4.41\ 10^9\ \mathrm{T}$. Above this value the field can no longer be described classically, and we should expect a significant production of electron-positron pairs [76]. Another invariant parameter that quantifies the effects of radiation reaction on the trajectories of leptons is $\chi = |F^{\mu\nu}p_\nu| / (E_{\mathrm{cr}}m)$, where $F^{\mu\nu}$ is the EM field tensor and p_ν is the corresponding particle four-momentum. The larger its value, the greater the differences between the quantum and classical predictions of radiation emission. It is also equal to the ratio of the electric field in the instantaneous rest frame of the electron to the critical field E_{cr}. Classically the frequency spectrum has no upper limit, whereas in the quantum case, there is a cutoff that ensures the frequency $\omega < \gamma m$. An analogous parameter χ_γ exists for the case of photons interacting with fields.

In the "moderately quantum" regime, when $\chi_\gamma < 1$, one can describe the radiation reaction through a variation of the Fokker-Planck equation [47]. The quantum photon emission can be thought of as a virtual inelastic collision between a laser photon and an electron, as long as the momentum exchange remains small compared with the emitting particle momentum. Quantum corrections to the spectrum become necessary when $\chi > 0.1$ and electron–positron pair creation and QED cascades are important when $\chi > 1$.

Normally one would resort to run full-3D-PIC simulations of a subset of the parameter space, avoiding low statistics of the electron beam macroparticles and ensure enough grid resolution for the laser dynamics to be correctly described. This direct approach consumes on the order of several million CPU-hours for each parameter set.

In the next chapter we will describe a semi-analytical method that partly mitigates this issue.

Chapter 3

Particle distributions according to the effective laser intensity they interact with

3.1 Positron production in a Plane Wave

The simplest description of a laser pulse is a plane wave with a temporal envelope. Such a wave is fully described by the wavelength λ, the pulse duration τ, and the normalized vector potential a_0, which relates to the intensity through $a_0 = 0.855\sqrt{I[10^{18}\ \mathrm{W/cm^2}]}\lambda[\mu\mathrm{m}]$ for linearly polarized lasers. As a relativistic electron interacts with this strong electromagnetic wavepacket, it emits (real) high-energy photons that can decay into electron-positron pairs through the Breit-Wheeler mechanism [77].

In the plane wave approximation, the total number of new pairs per interacting electron can be estimated if we know the initial electron energy $\gamma_0 mc^2$ (where γ_0 is the electron Lorentz factor, m the electron mass and c is the speed of light), and the laser parameters (peak a_0, central wavelength λ and pulse duration τ, which is defined as the full width at half maximum of the laser intensity pulse envelope). The total number of pairs is then given by [78]:

$$N_{+}^{\mathrm{PW}}(\gamma_0, a_0, \lambda, \tau) \simeq 3\sqrt{\frac{\pi}{2}} P_{\pm}(\omega_c)\ \chi_{\mathrm{c,rr}}\ \frac{(\gamma_0 mc^2 - \hbar\omega_c)^2}{\hbar\gamma_0 mc^2}\ \frac{\mathrm{d}N_\gamma}{\mathrm{d}\omega}\bigg|_{\omega=\omega_c} \tag{3.1}$$

The first term $P_{\pm}(\omega_c)$ represents the total probability of a photon of frequency ω_c producing an electron-positron pair when colliding with the pulsed laser plane wave; the second is the recoiled $\chi_{\mathrm{c,rr}}$ which accounts for the radiation reaction on the beam electrons, and the final term $\mathrm{d}N_\gamma/\mathrm{d}\omega$ is the photon distribution emitted by the electron beam, evaluated at the frequency $\omega = \omega_c$. This approximated photon spectrum underestimates the number of low-energy photons, but should not significantly affect the positron production calculation for relatively low χ_e regime. According to this model, all positrons are generated from photons with a critical frequency ω_c, and there is no feedback by the produced pairs on the photon spectra (in other words, there is only one generation of secondary particles). Furthermore, the model assumes a semi-classical equation of motion of the electrons as they lose energy through the emission of radiation and uses the locally constant field [79] and rigid-beam approximations.

Unfortunately, many of the terms in equation 3.1 are implicit functions of its four parameters, which invalidate any effort to use it directly for analytical calculations. It could be possible to fit this function by a simpler model; however, we choose to use this original form throughout this work and resort to numerical computations whenever necessary.

3.2 Beyond Plane Wave

Let us now consider a focused laser pulse illustrated in figure 1.2. The maximum laser intensity an individual particle within the electron beam interacts with depends on two geometrical factors: the transverse offset from the laser axis compared to the laser spotsize and the initial longitudinal position that affects the temporal synchronization of the interaction. In other words, while interacting with a focused laser pulse, electrons far from the focus interact with a lower average (and peak) field, which must be taken into account.

The effective vector potential for a Gaussian laser has the following spatial dependence

$$a_{0,\mathrm{eff}} = \frac{a_0}{\sqrt{1+(z/z_R)^2}} \exp\left(-\frac{(x^2+y^2)/W_0^2}{1+(z/z_R)^2}\right) \tag{3.2}$$

where z is the coordinate along the optical axis and (x, y) are the transverse coordinates, a_0 is the peak vector potential, λ the laser wavelength, W_0 is the transverse spot size, and $z_R \equiv \pi W_0^2/\lambda$ the Rayleigh-range. Lasers in experiments rarely correspond to an idealized Gaussian beam; however, this is a common starting point for many theoretical models.

The electron encounters the peak of the laser pulse at time t in a (x, y, z) point of configuration space which defines the maximum field felt by this particle. We can therefore assign an effective vector potential $a_{0,\mathrm{eff}}(t, x, y, z)$ that corresponds to the maximum laser intensity the particle experiences during the interaction.

In [78] and [80], this idea was used to compute the total number of positrons produced by disk beams of zero length, assuming the collision occurred in the focal plane, through integration in coordinate space

$$N_+ = \int N_+^{\mathrm{PW}}(a_{0,\mathrm{eff}}(\vec{r}))\, n_b(\vec{r})\, \mathrm{d}\vec{r} \tag{3.3}$$

However, for analytical calculations, this approach will most likely require approximations, namely the saddle-point method. We follow a different path, which will prove more useful in more complex geometries. We define an equivalent distribution of beam particles according to the maximum intensity they interact with during the scattering.

In the case of a Plane Wave interaction, as there is no defocusing, all particles interact with the same intensity, regardless of where or when they overlap with the peak of the laser a_0, and the equivalent distribution would be a Dirac Delta function $\delta(a_{0,\mathrm{eff}} - a_0)$. In the case of a focused laser, the distribution is no longer a Delta function but has some spread in the range of possible values $a_{0,\mathrm{eff}} \in [0, a_0]$.

The problem can be addressed using cylindrical coordinate system (ρ, ϕ, z), centered at the laser focus. For a Gaussian laser beam (in the paraxial approximation), the configuration space can be mapped to the laser intensity isosurfaces shown in figure 3.1, which are invariant on the coordinate ϕ. For simplicity's sake, let us first assume that the electron beam is a cylinder with a constant density n_b. Each particle meets the laser beam at a different point of space, and is assigned $a_{0,\mathrm{eff}}(\rho, z)$, where ρ and z are its coordinates at the instant of time when it is synchronised with the peak of the laser. Performing a one-to-one mapping to the new coordinates of a flat-top relativistic beam in counter-propagation with the laser, the beam density in the new coordinates doubles, and the length shrinks by two because the laser-electron crossing happens at twice the speed of light.

One way of exactly computing the distribution of particles is through

$$\frac{\mathrm{d}N_b(a_{0,\mathrm{eff}})}{\mathrm{d}a_{0,\mathrm{eff}}}(a_{0,\mathrm{eff}}) = \int_V 2n_b(\vec{r})\ \delta(a_{0,\mathrm{eff}} - a_{0,\mathrm{eff}}(\vec{r}))\ \mathrm{d}\vec{r} \tag{3.4}$$

where the Delta function selects the correct $a_{0,\mathrm{eff}}$ isosurface. Although this approach can be used numerically or to perform analytical calculations, there is a much simpler alternative approach.

The number of particles $\mathrm{d}N_b(a_{0,\mathrm{eff}})$ with $a_{0,\mathrm{eff}}$ that falls in the interval $[a_{0,\mathrm{eff}}, a_{0,\mathrm{eff}} + \mathrm{d}a_{0,\mathrm{eff}}]$ can then be estimated to be $\mathrm{d}N_b(a_{0,\mathrm{eff}})/\mathrm{d}a_{0,\mathrm{eff}} = 2n_b\ \mathrm{d}V/\mathrm{d}a_{0,\mathrm{eff}}$, where $\mathrm{d}V$ is the volume between two adjacent isosurfaces associated with $a_{0,\mathrm{eff}}$ and $a_{0,\mathrm{eff}} + \mathrm{d}a_{0,\mathrm{eff}}$. Due to the geometry of the problem, this expression can be transformed to the following:

$$\frac{\mathrm{d}N_b(a_{0,\mathrm{eff}})}{\mathrm{d}a_{0,\mathrm{eff}}} = \int_S \frac{2n_b\ \mathrm{d}S}{||\nabla a_{0,\mathrm{eff}}||} \tag{3.5}$$

where the surface element $\mathrm{d}S = \rho\sqrt{\mathrm{d}\rho^2 + dz^2}\ \mathrm{d}\phi = \rho\sqrt{1 + (\partial\rho/\partial z)^2}\ \mathrm{d}z\ \mathrm{d}\phi$ is calculated at the isosurface that is by definition perpendicular to the gradient of the vector potential given by $||\nabla a_{0,\mathrm{eff}}|| = \sqrt{(\partial a_{0,\mathrm{eff}}/\partial\rho)^2 + (\partial a_{0,\mathrm{eff}}/\partial z)^2}$.

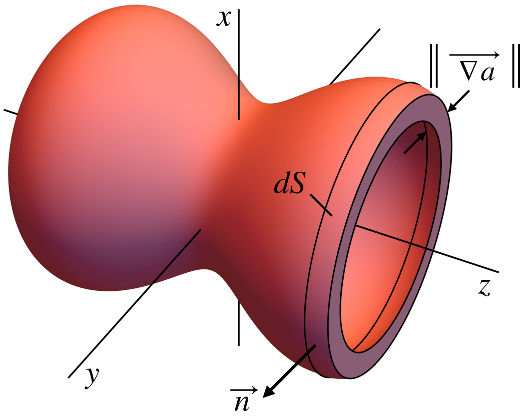

Figure 3.1: A volume element between two isosurfaces of the effective normalized vector potential $a_{0,\mathrm{eff}}$. The volume element contains all the points where particles experience the peak a_0 within the interval $[a_{0,\mathrm{eff}}, a_{0,\mathrm{eff}} + \mathrm{d}a_{0,\mathrm{eff}}]$.

It may seem we have gained little by using this approach; however, we have traded a 3D integral (which would usually require heavier computations) with a 1D integral. Even if the scaling law (in this case N_+^{PW}) is not easy to integrate explicitly, from the numerical point of view, our approach allows for faster numerical integration. It also provides intuition on the influence of the beam geometry on the particle distribution. Once the particle distribution in equation (3.5) is calculated, we can extract field moments $\langle {a_{0,\mathrm{eff}}}^k \rangle = \int {a_{0,\mathrm{eff}}}^k \, \mathrm{d}N/\mathrm{d}a_{0,\mathrm{eff}} \, \mathrm{d}a_{0,\mathrm{eff}}$, which can for example be used to calculate the average laser intensity [51].

Letting beam electron density vary in space $n_b(\vec{r})$ allows considering cases of short or long, wide or narrow beams, including non-ideal spatio-temporal synchronization with the laser (as discussed later for cases illustrated in figure 3.2). It is worth noting that even a point-particle interaction with a Gaussian beam is not equivalent to a plane wave approximation unless the particle is in perfect temporal synchronization with the laser pulse.

For a more general case, by considering a corrected $a_{0,\mathrm{eff}}$ for each particle, we can apply the equations already derived for a plane wave (equation 3.1), and then integrate over the distribution function in $a_{0,\mathrm{eff}}$ to obtain the total yield of positrons in the laser-electron scattering. The integration can be performed by sampling the distribution function numerically or performing an analytical integration over the configuration space in cases where this is possible. While in [78] the authors calculate the total number of positrons by analytically or numerically integrating the scaling law for the plane wave in coordinate space (x, y, z) or (z, ρ, ϕ), in this work we are only required to calculate a 1-dimensional integral in $a_{0,\mathrm{eff}}$-space after deriving the distribution of particles $\mathrm{d}N/\mathrm{d}a_{0,\mathrm{eff}}$.

An alternative way to obtain the distribution of particles in $a_{0,\mathrm{eff}}$ is to numerically sample the electron beam density $n_b(z, \rho, \phi)$ in space (the “sampling” method). The sampled distribution function can be directly binned into a histogram according to the maximum value of a_0 each section interacts with. This allows to take into account arbitrary beam shapes and include spatial structures like correlated energy chirp that can be present in LWFA beams. As long as the equation 3.1 for the number of expected pairs in a plane wave interaction is correct, the “sampling” method is expected to predict a correct result for a focused Gaussian laser beam interacting with an electron beam of any shape and size. We use it to verify the explicit distribution functions obtained analytically for several typical cases expected in an experiment. A good agreement between the predictions of the two methods confirms that the analytical distribution functions are correct and that the approximations taken in the electron beam description are valid. Even in cases where the field structure is too intricate for simple, explicit analytical calculations, one can always adopt the sampling approach.

The total number of positrons will then be a weighted integral of the scaling law for the plane wave 3.1

$$N_+ = \int N_+^{\mathrm{PW}}(a_{0,\mathrm{eff}}) \, \frac{\mathrm{d}N}{\mathrm{d}a_{0,\mathrm{eff}}}(a_{0,\mathrm{eff}}) \, \mathrm{d}a_{0,\mathrm{eff}} \tag{3.6}$$

As a first application of the ideas presented in this section, let us consider the scattering between a focused Gaussian laser pulse and a short Gaussian electron beam.

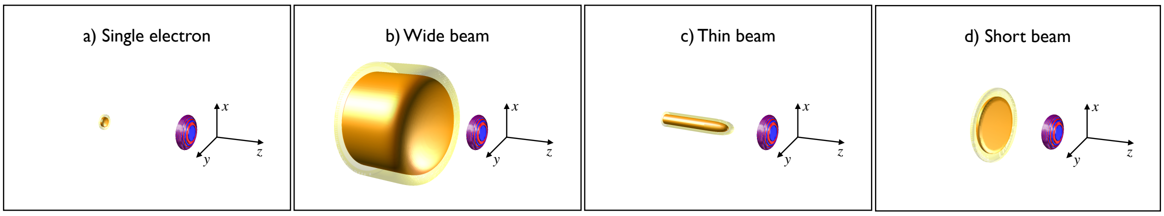

Figure 3.2: Scattering with nontrivial electron beam shapes. a) A single electron-laser interaction equivalent to electron colliding with a plane wave packet ($L \ll z_R,\ R \ll W_0$). b) Interaction with a wide electron beam ($R \gg W_0$). c) Interaction with a pencil-like thin electron beam ($R \ll W_0$). d) Interaction with a short electron beam ($L \ll z_R$).

3.3 Short beam

In Ref. [78], the authors consider a spherically-symmetric Gaussian beam profile with a radius $R = 6\ \mu\mathrm{m}$, a laser spotsize of $W_0 = 2\ \mu\mathrm{m}$ and a Rayleigh range $z_R = 15.7\ \mu\mathrm{m}$. As the Rayleigh range is much higher than the beam length ($z_R \gg R$), one can consider the beam short. In this same paper, an approximate expression for the expected value of the number of positrons is obtained, which correctly predicts the order of magnitude, but differs by a factor of two compared with the simulation they ran. This motivates the use of our method to better estimate this quantity.

Let us define a short beam $L \ll z_R$ beam (effectively of zero length) with a transverse Gaussian density profile $n_b = n_0 \exp\left(-((x - \Delta_\perp)^2 + y^2)/R^2\right)$ where the peak density is given by $n_0 = N_b/(\pi R^2 L)$, $x = \rho \cos\phi$ and $y = \rho \sin\phi$. We assume a longitudinally synchronized beam ($\Delta_{||} = 0$), with an allowed transverse displacement $\Delta_\perp$ between the beam centre and the laser propagation axis. The electrons therefore interact with the laser peak at $z = 0$ and the field structure reduces to $a_{0,\mathrm{eff}} = a_0 \exp\left(-\rho^2/W_0^2\right)$. As the manifolds of constant $a_{0,\mathrm{eff}}$ are now concentric rings, the volume element associated with a specific value of $a_{0,\mathrm{eff}}$ is given by $\mathrm{d}V = L\ \rho\ \mathrm{d}\rho\ \mathrm{d}\phi/2$, the surface element of an isosurface is $\mathrm{d}S = L\ \rho\ \mathrm{d}\phi/2$, and the field gradient is given by $\nabla a_{0,\mathrm{eff}} = \partial a_{0,\mathrm{eff}}/\partial\rho\ \hat{\rho}$, with $\partial a_{0,\mathrm{eff}}/\partial\rho = -2\rho\ a_{0,\mathrm{eff}}/W_0^2$. We can now apply the equation (3.5) to obtain the particle distribution function $\mathrm{d}N_b(a_{0,\mathrm{eff}})/\mathrm{d}a_{0,\mathrm{eff}} = \int L\ n_b\ \rho\ \mathrm{d}\phi/||\nabla a_{0,\mathrm{eff}}||$. This gives

$$\frac{\mathrm{d}N_b}{\mathrm{d}a_{0,\mathrm{eff}}} = \frac{L n_0 W_0^2}{2 a_{0,\mathrm{eff}}}\ e^{-\rho^2/R^2}\ e^{-\Delta_\perp^2/R^2} \int_0^{2\pi} e^{2\rho\Delta_\perp \cos\phi/R^2} \mathrm{d}\phi \tag{3.7}$$

where $-\rho^2 = W_0^2 \log(a_{0,\mathrm{eff}}/a_0)$ and the integration result can be expressed through the modified Bessel function of the first kind $I_0(t) \equiv (1/\pi) \int_0^\pi \exp(t\cos\phi)\mathrm{d}\phi$.

The obtained particle distribution function is given in Table 3.1. One can now numerically integrate the previous histogram distribution with N_+^{PW}. This leads to results consistent with the simulation data of Ref. [78]. Detailed comparisons are shown in figure 3.3.

Having proved consistency with previously published results, we now move on to finite length beams in the next sections.

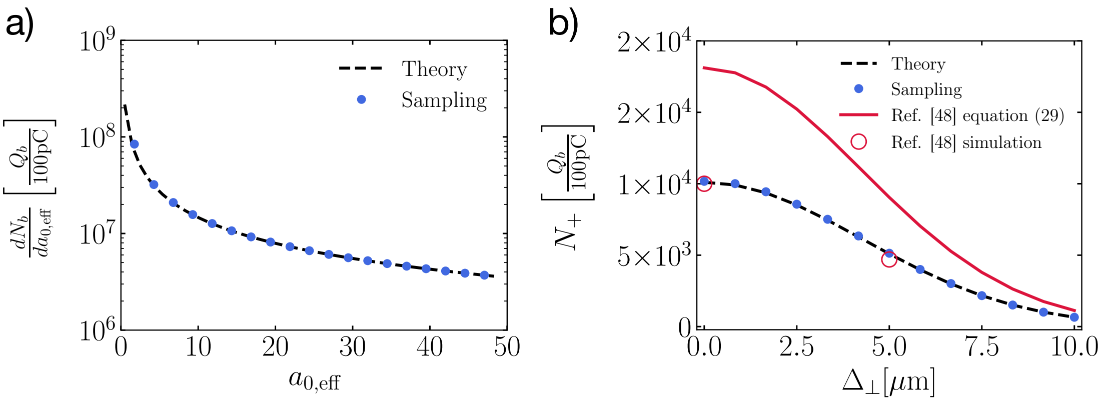

Figure 3.3: Short beam. a) Particle distribution according to the effective vector potential for a transversely aligned beam ($\Delta_\perp = 0$). b) Positron yield as a function of transverse beam displacement from the laser propagation axis $\Delta_\perp$. The electron beam energy is $E_0 = 2$ GeV, charge is $Q_b = 100$ pC and Gaussian radius $R = 6\ \mu$m in all spatial directions. The laser parameters are $a_0 = 48.4, \lambda = 0.8\ \mu\mathrm{m}, \tau = 30$ fs and $W_0 = 2\mu$m.

3.4 Thin beam

For LWFA beams, if the scattering is performed within the wakefield bubble where the electron beam transverse size is $\sim 2\ \mu$m, we can adopt a new geometry which we call Thin. In this model, the beam length is arbitrary, and the radius is much smaller than the laser spotsize $R \ll W_0$ such that we consider it zero. Therefore, the problem becomes one-dimensional and the number of particles associated with a specific value of intensity is given by $\mathrm{d}N_b = 2n_b\,\mathrm{d}V = 4(N_b/L)\,\mathrm{d}z$. The effective laser intensity depends only on z through $a_{0,\mathrm{eff}}(z) = a_0/\sqrt{1+(z/z_R)^2}$ and the distribution becomes

$$\frac{\mathrm{d}N_b}{\mathrm{d}a_{0,\mathrm{eff}}} = \frac{4N_b}{L}\frac{\mathrm{d}z}{\mathrm{d}a_{0,\mathrm{eff}}}. \tag{3.8}$$

The explicit distribution is given in Table 3.1.

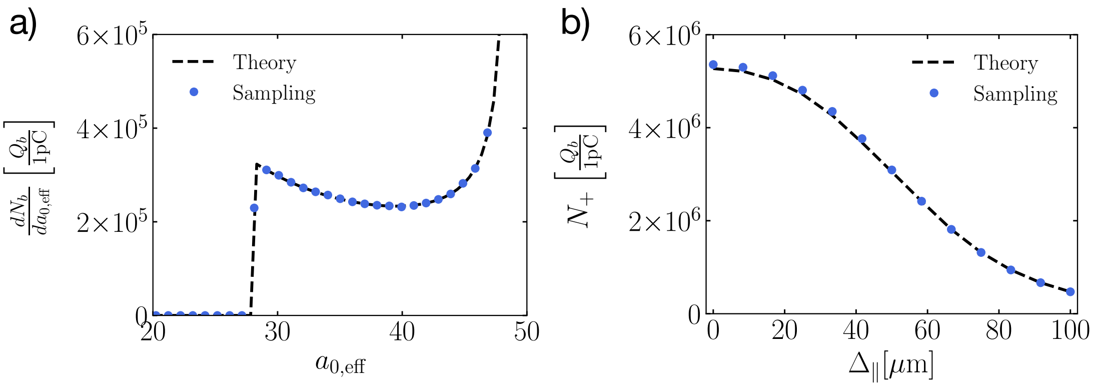

Figure 3.4: Thin beam. a) Particle distribution according to the effective vector potential for $\Delta_\parallel = 0$. b) Positron yield as a function of temporal synchronization. The beam energy is $E_0 = 13$ GeV, charge is $Q_b = 1$ pC and length $L = 200\ \mu$m. The laser parameters are $a_0 = 48.4,\ \lambda = 0.8\ \mu\mathrm{m},\ \tau = 35$ fs, $W_0 = 3\ \mu$m and $\Delta_\parallel$ represents the longitudinal displacement of the beam centre when the laser is at the focus.

3.5 Wide beam

Although LWFA beams can be very narrow immediately after acceleration within the plasma, the scattering can occur a few cm away from this position. If the beam has some momentum divergence, its transverse size will increase as it propagates towards the laser's focus. In some cases, the beam radius can become much larger than the laser spotsize. This can also happen with electron beams produced by conventional accelerators (e.g., [81]).

Let us define a Wide beam as one where beam radius is much larger than the laser focal spot W_0 (opposite limit from the Thin beam), such that any transverse density profile can be approximated as a uniform one. The gradient of $a_{0,\mathrm{eff}}$ can be written as $||\nabla a_{0,\mathrm{eff}}|| = |\partial a_{0,\mathrm{eff}}/\partial\rho|\ \sqrt{1+(\partial\rho/\partial z)^2}$, where $|\partial a_{0,\mathrm{eff}}/\partial\rho| = 2\rho\ a_{0,\mathrm{eff}}/(W_0^2(1+(z/z_R)^2))$. This simplifies the particle distribution according to equation (3.5):

$$\frac{\mathrm{d}N_b(a_{0,\mathrm{eff}})}{\mathrm{d}a_{0,\mathrm{eff}}} = \frac{2\pi\ n_b\ W_0^2}{a_{0,\mathrm{eff}}} \int_{z_{\min}}^{z_{\max}} 1 + \left(\frac{z}{z_R}\right)^2 \mathrm{d}z \tag{3.9}$$

where the limits of integration in z direction will depend on the beam length and its temporal synchronization with the laser pulse. If the entire isosurface associated with a specific $a_{0,\mathrm{eff}}$ is covered with interacting particles, $z_{\max} = -z_{\min} = z_R\sqrt{(a_0/a_{0,\mathrm{eff}})^2 - 1}$. Otherwise, a portion of the volume associated with a specific laser intensity may be empty due to the finite beam length and temporal synchronization. For every $a_{0,\mathrm{eff}}$, one has to evaluate what the appropriate integration limits are on each side. There is a transition in the distribution function at $a_z \equiv a_0/\sqrt{1+(L/4z_R)^2}$ (above which the isosurfaces are full) that corresponds to the beam edge on-axis, as shown by the examples in figure 3.5a). The distribution function for a wide, flat-top electron beam is given explicitly in Table 3.1.

We now illustrate the obtained particle distributions according to the effective laser intensity with an example. The SFQED experiment [57] will study pair-production using a 0.61 J laser pulse ($a_0 = 7.3$, $\lambda = 0.8\ \mu\mathrm{m}$, $W_0 = 3\ \mu\mathrm{m}$, $\tau = 35\ \mathrm{fs}$) and a $13\mathrm{GeV}$, $2\ \mathrm{nC}$ electron beam. The electron beam follows a non-symmetric Gaussian density distribution transversely with $\sigma_x = 24.4\ \mu\mathrm{m}$, $\sigma_y = 29.6\ \mu\mathrm{m}$, and has a $\sim 250\ \mu\mathrm{m}$ long flat-top longitudinal profile.

To save computing time, we performed 3D PIC simulations of this interaction using OSIRIS [70] by dividing the long beam into five equal beamlets each $50.9\ \mu\mathrm{m}$ long. These beamlets have different temporal synchronization (they encounter the laser peak at different distances from the focus). The 3D simulations are performed with a box size of $98\ \mu\mathrm{m} \times 25\ \mu\mathrm{m} \times 25\ \mu\mathrm{m}$, resolved with $3840 \times 400 \times 400$ cells. OSIRIS PIC results (red empty circles in figure 3.5 b)) are compared with the analytical predictions based on above intensity distribution functions and a numerically sampled beam. The distribution functions for the temporally non-synchronised electron beam with $\Delta_{\parallel} \neq 0$ are shown in table 3.2.

For the analytical calculations and numerical sampling, we assumed the beam has a uniform density equal to the central density of the electron beam $n_b = 10^{16}\ \mathrm{cm}^{-3}$. This is justified by $\sigma_x \gg W_0$ and $\sigma_y \gg W_0$, and the highest intensity portion interacts nearly exclusively with the maximum density of the beam. Therefore, the analytical calculation is coherent with the simulation results, as confirmed by the comparison in figure 3.5 b).

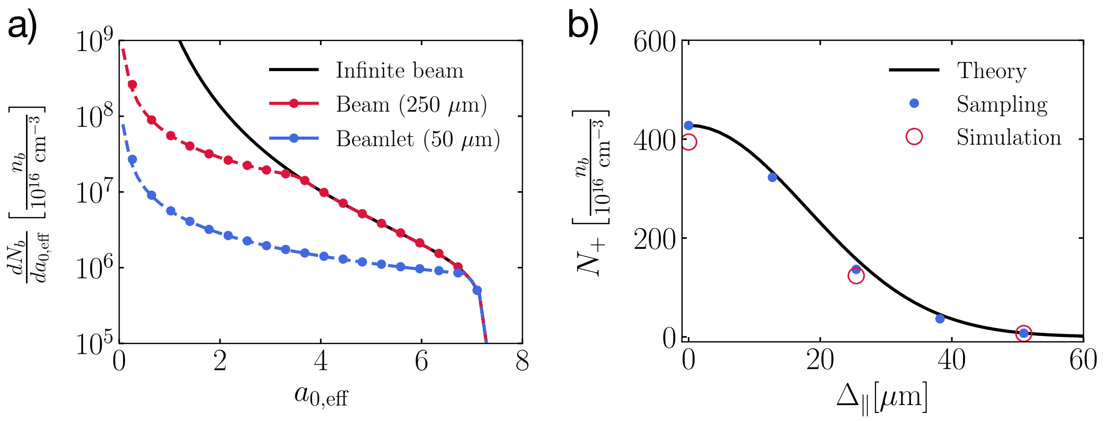

Figure 3.5: Wide beam. a) Particle distribution according to the effective laser vector potential $a_{0,\mathrm{eff}}$. Dashed lines are analytical expressions, circles are from sampling and full line corresponds to the limiting case of $L \to \infty$. b) Positron yield as a function of the longitudinal displacement $\Delta_\parallel$ for one beamlet. The laser parameters are $a_0 = 7.3$, $\lambda = 0.8\ \mu\mathrm{m}$, $\tau = 31\ \mathrm{fs}$ and $W_0 = 3\ \mu\mathrm{m}$. The beam energy is $E_0 = 13\ \mathrm{GeV}$, transverse width $\sigma_x = 24.4\ \mu\mathrm{m}$ and $\sigma_y =\ 29.6\ \mu\mathrm{m}$. The beam length is $L = 50.9\ \mu\mathrm{m}$ for each beamlet, while the entire beam contains $Q = 2\ \mathrm{nC}$ and is $250\ \mu\mathrm{m}$-long.

3.5.1 Alternative derivation of the particle distribution

In this section we derive the particle distribution for a Wide beam in an alternative way. Because of the crossing with the laser, the effective length of the beam shortens in half. Therefore, for a temporally synchronized scattering, electrons are mapped to a region $z \in [-L/4, +L/4]$.

To keep notation short we'll use $a \equiv a_{0,\mathrm{eff}} \leq a_0$ and normalize variables as $\bar{a} = a/a_0$, $\bar{\rho} = \rho/W_0$, $\bar{z} = z/z_R$. The spatial distribution of the laser field then follows

$$\bar{a} = \frac{1}{\sqrt{1+\bar{z}^2}} \exp\left(-\frac{\bar{\rho}^2}{1+\bar{z}^2}\right)$$

It will be easier to work with the square of the field

$$\bar{a}^2 = \frac{1}{1+\bar{z}^2} \exp\left(-\frac{2\bar{\rho}^2}{1+\bar{z}^2}\right)$$

To integrate out the coordinates we will need to write one of the coordinates as a function of the other plus $\bar{a}$. We cannot do this explicitly for z, so the remaining option is to write $\rho = \rho(a, z)$. This then becomes

$$(1+\bar{z}^2)\bar{a}^2 = \exp(-2\bar{\rho}^2(1+\bar{z}^2)^{-1}) \Leftrightarrow -2\bar{\rho}^2 = (1+\bar{z}^2)\log(\bar{a}^2(1+\bar{z}^2)) \tag{3.10}$$

In cylindrical coordinates (z, ρ, ϕ) the element surface will be of the form $(\mathrm{d}S)^2 = \rho^2\left(1 + (\partial\rho/\partial z)^2\right)(\mathrm{d}z)^2(\mathrm{d}\phi)^2$. Because of cylindrical symmetry, integration in ϕ is trivial and gives 2π.

Using expression 3.10 we get

$$-2\frac{\partial\bar{\rho}^2}{\partial\bar{z}^2} = 1 + \log(\bar{a}^2(1+\bar{z}^2)) = 1 - 2\bar{\rho}^2(1+\bar{z}^2)^{-1}$$

This can then be used in

$$\left(\frac{\partial\bar\rho}{\partial\bar z}\right)^2 = \frac{\bar z^2}{\bar\rho^2}\left(\frac{\partial\bar\rho^2}{\partial\bar z^2}\right)^2 = \frac{\bar z^2}{4\bar\rho^2}\frac{(1+\bar z^2-2\bar\rho^2)^2}{(1+\bar z^2)^2}$$

Finally, the elemental surface becomes

$$\frac{1}{W_0^2\bar\rho^2}\frac{(\mathrm{d}S)^2}{(\mathrm{d}z)^2} = 1 + \frac{W_0^2}{4z_R^2}\frac{\bar z^2}{\bar\rho^2}\frac{(1+\bar z-2\bar\rho^2)^2}{(1+\bar z)^2} \tag{3.11}$$

The gradient in cylindrical coordinates is $\nabla a = (\partial a/\partial\rho)\hat\rho + (\partial a/\partial z)\hat z$ so $||\nabla a||^2 = (\partial a/\partial\rho)^2 + (\partial a/\partial z)^2$. Using the same strategy as with the elemental surface, we first calculate

$$\frac{\partial\bar a^2}{\partial\bar\rho^2} = \frac{-2\bar a^2}{1+\bar z^2}, \quad \frac{\partial\bar a^2}{\partial\bar z^2} = \frac{-\bar a^2(1+\bar z^2-2\bar\rho^2)}{(1+\bar z^2)^2}$$

Then the ρ component of the gradient becomes

$$\left(\frac{\partial a}{\partial\rho}\right)^2 = \frac{a_0^2}{W_0^2}\left(\frac{\partial\bar a}{\partial\bar\rho}\right)^2 = \frac{a_0^2}{W_0^2}\left(\frac{\bar\rho}{\bar a}\right)^2\left(\frac{\partial\bar a^2}{\partial\bar\rho^2}\right)^2$$

and similarly for $\left(\frac{\partial\bar a}{\partial\bar z}\right)^2$. Combining these results

$$\frac{W_0^2\bar a^2}{a_0^2}||\nabla a||^2 = \bar\rho^2\left(\frac{\partial\bar a^2}{\partial\bar\rho}\right)^2 + \bar z^2\frac{W_0^2}{z_R^2}\left(\frac{\partial\bar a^2}{\partial\bar z}\right)^2 \Leftrightarrow$$

$$\frac{(1+\bar z^2)^2}{4\bar\rho^2\bar a^4}\frac{W_0^2\bar a^2}{a_0^2}||\nabla a||^2 = 1 + \frac{W_0^2}{4z_R^2}\frac{\bar z^2}{\bar\rho^2}(1+\bar z^2-2\bar\rho^2)^2$$

which is very similar to 3.11 and will simplify calculations. As the density profile is flat $n_b = n_0$, then

$$\frac{\mathrm{d}S/\mathrm{d}z}{||\nabla a||} = \frac{W_0^2}{2a}\left(1+\frac{z^2}{z_R^2}\right)$$

Integrating in z gives us

$$\frac{\mathrm{d}N}{\mathrm{d}a} = \frac{W_0^2}{2a}\left(z+\frac{z^3}{3z_R^2}\right)\Bigg|_{-z_{\max}}^{+z_{\max}}$$

where $z_{\max} = z_R\sqrt{a_0^2/a^2-1}$ is the maximum z for each isosurface along the optical axis $\rho = 0$.

In table 3.1 we gather the analytical expressions of the particle distributions for the previous geometries.

3.6 Detailed particle distribution functions in centered and non-centered laser collisions

In this section, we derive the distribution of particles for an arbitrary temporal synchronization. Similarly, as for the synchronized beams, we map the individual beam particles according to the spatial positions

Setup	Particle distribution for temporally centered beams
Wide beam	$\frac{\mathrm{d}N_b}{\mathrm{d}a_{0,\text{eff}}} = \begin{cases} \frac{4\pi\ n_b\ W_0^2\ z_R}{a_{0,\text{eff}}} \frac{\sqrt{a_0^2 - a_{0,\text{eff}}^2}}{3a_{0,\text{eff}}} \left(2 + \left(\frac{a_0}{a_{0,\text{eff}}}\right)^2\right), a_{0,\text{eff}} \geq a_z \\ \frac{4\pi\ n_b\ W_0^2\ z_R}{a_{0,\text{eff}}} \frac{L}{4z_R} \left(1 + \left(\frac{L}{4z_R}\right)^2\right), a_{0,\text{eff}} < a_z \end{cases}$
Thin beam	$\frac{\mathrm{d}N_b}{\mathrm{d}a_{0,\text{eff}}} = \begin{cases} \frac{4N_b z_R}{L} \frac{a_0^2}{a_{0,\text{eff}}^2} \frac{1}{\sqrt{a_0^2 - a_{0,\text{eff}}^2}}, a_{0,\text{eff}} \geq a_z \\ 0, a_{0,\text{eff}} < a_z \end{cases}$
Short beam	$\frac{\mathrm{d}N_b}{\mathrm{d}a_{0,\text{eff}}} = \frac{N_b\ W_0^2}{R^2\ a_{0,\text{eff}}} \left(\frac{a_{0,\text{eff}}}{a_0}\right)^{(W_0/R)^2} e^{-\Delta_\perp^2/R^2}\ I_0\left(\frac{2\Delta_\perp W_0}{R^2}\sqrt{\log\left(\frac{a_0}{a_{0,\text{eff}}}\right)}\right)$

Table 3.1: Particle distributions according to the effective vector potential for different beam geometries. Here, $a_z \equiv a_0/\sqrt{1+(L/4z_R)^2}$ is the $a_{0,\text{eff}}$ associated with the integration limits imposed by the longitudinal size of the electron beam, N_b represents the total number of particles in the beam, n_b is the beam density, R and L are the beam radius and length respectively. The laser spot size is W_0, $z_R \equiv \pi W_0^2/\lambda$ is the Rayleigh length, $\Delta_\perp$ is the perpendicular displacement of the beam centre from the laser propagation axis, and I_0 is a Bessel function of the first kind.

where they encounter the peak of the laser pulse. The temporal synchronization is then quantified through a longitudinal offset of the electron beam center from the focal plane given by $\Delta_{\parallel}$. Without the loss of generality, we assume that $\Delta_{\parallel} > 0$.

Whereas before the boundaries of the electron beam were mapped to $z_\pm = \pm L/4$, now they are shifted to $z_\pm = \pm L/4 + \Delta_{\parallel}$. To obtain a distribution function, one needs to reevaluate the integral on the RHS of equation 3.5 between z_- and z_+. This integration can be performed formally, but we present a more intuitive calculation relying on geometry.

The beam can be divided into two parts: the blue part on the LHS of the focal plane and the yellow part on the RHS of the focal plane. This can be interpreted as follows: the total distribution in $a_{0,\text{eff}}$ can then be written as a sum of the distributions coming from the blue and the yellow sections of the beam. Each of these beams contributes with exactly half of the distribution function associated with a symmetrical (temporally synchronized) beam twice its size. This means we can re-use the distribution functions, modifying the beam lengths to $|z_-|$ and $|z_+|$. For a large temporal offset $\Delta_{\parallel} > L/4$, none of the beam particles interact with the laser in the focus (this is illustrated in figure 3.6 b)). In this case, we subtract the contribution of the blue beam from the contribution of the yellow beam. This reasoning applies both to thin and wide beam geometries.

In the case of a short beam, the maximum interaction value for $a_{0,\text{eff}}$ will be determined by the distance from the focus through $a_{\parallel} = a_0/\sqrt{1+(\Delta_{\parallel}/z_R)^2}$, and the effective spotsize becomes $W(\Delta_{\parallel}) = W_0\sqrt{1+(\Delta_{\parallel}/z_R)^2}$. The modified distribution functions in $a_{0,\text{eff}}$ including the temporal offset were collected in table 3.2 for easy reference.

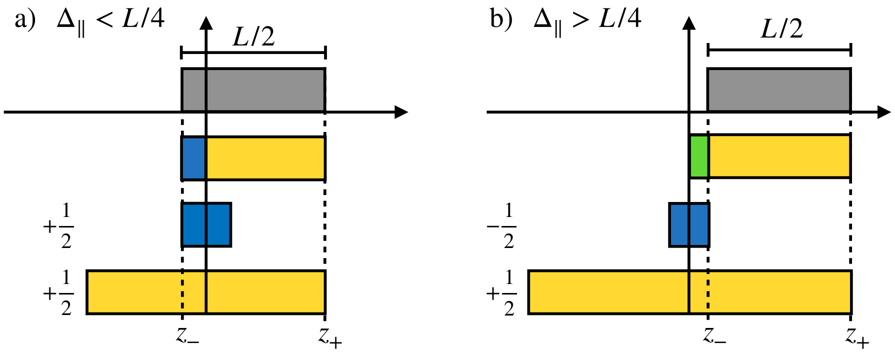

Figure 3.6: a) A partially synchronized electron beam. b) Electron beam with a large temporal offset. The beam represented in grey can be expressed as a linear combination of the beams represented in blue and yellow.

Setup	Particle distribution for temporally unsynchronized beams
Wide beam	$\frac{\mathrm{d}N_b}{\mathrm{d}a_{0,\text{eff}}} = \frac{2\pi\, n_b\, W_0^2\, z_R}{a_{0,\text{eff}}} \left(\frac{z_+}{z_R}\left(1+\frac{1}{3}\left(\frac{z_+}{z_R}\right)^2\right)\theta(a_{z_+}-a_{0,\text{eff}}) - \frac{z_-}{z_R}\left(1+\frac{1}{3}\left(\frac{z_-}{z_R}\right)^2\right)\theta(a_{z_-}-a_{0,\text{eff}}) + \frac{\sqrt{a_0^2-a_{0,\text{eff}}^2}}{3\, a_{0,\text{eff}}}\left(2+\frac{a_0^2}{a_{0,\text{eff}}^2}\right)\left(\theta(a_{0,\text{eff}}-a_{z_+}) \pm \theta(a_{0,\text{eff}}-a_{z_-})\right)\right)$
Thin beam	$\frac{\mathrm{d}N_b}{\mathrm{d}a_{0,\text{eff}}} = \frac{2N_b z_R}{L}\,\frac{a_0^2}{a_{0,\text{eff}}^2}\,\frac{1}{\sqrt{a_0^2-a_{0,\text{eff}}^2}}\left(\theta(a_{0,\text{eff}}-a_{z_+}) \pm \theta(a_{0,\text{eff}}-a_{z_-})\right)$
Short beam	$\frac{\mathrm{d}N_b}{\mathrm{d}a_{0,\text{eff}}} = \frac{N_b\, W_0^2}{R^2\, a_{0,\text{eff}}}\left(\frac{a_{0,\text{eff}}}{a_0}\sqrt{1+\left(\frac{\Delta_\parallel}{z_R}\right)^2}\right)^{\left(\frac{W_0}{R}\right)^2\left(1+\left(\frac{\Delta_\parallel}{z_R}\right)^2\right)}$, if $a_{0,\text{eff}} < a_\parallel$

Table 3.2: Particle distributions for arbitrary temporal synchronization. The $\pm$ sign corresponds to situations where $\Delta_\parallel < L/4$ or $\Delta_\parallel > L/4$ respectively, and $z_\pm = \Delta_\parallel \pm L/4$. $\theta(x)$ is the Heaviside Theta function, $a_{z_\pm} = a_0/\sqrt{1+(z_\pm/z_R)^2}$ and $a_\parallel = a_0/\sqrt{1+(\Delta_\parallel/z_R)^2}$.

3.7 Observations

In the case of a Short beam, we are not making any additional assumptions from the approach carried out in [78, 80]. Therefore, it is not surprising that our method is consistent with the results of those papers. However, to the best of our knowledge, this Thesis is the first work to extend this approach to finite length beams, where we assume that we can apply the same reasoning as in the Short beam to each infinitesimally thin slice of electrons in Thin and Wide beams.

In the case of a Wide beam, one cannot normalize the distribution function as in the previous cases by integration in $a_{0,\mathrm{eff}} \in [0, a_0]$, because, as we consider a uniform electron density in the transverse plane, the total number of particles within an isosurface would diverge as $a_{0,\mathrm{eff}} \to 0$. Instead, proper normalization of the distribution (in the sense that this will accurately map to a histogram) is achieved by considering the number of particles within isosurfaces in the limit limit $a_{0,\mathrm{eff}} \to a_0$.

In the case of the positron yield, N_+^{PW} is a super-polynomial function of a_0 (will go to zero faster than any polynomial of a_0 as $a_0 \to 0$), which means that even for unnormalizable distribution functions such as for the Wide beam, the global positron yield will not diverge.

Another assumption made for the Wide beam case is that the isosurfaces never cross the transverse boundary of the beam. If that were to occur (for a finite beam radius), we would have to define more branches of the distribution.

The distributions in this chapter were derived for geometries with cylindrical symmetry. However, realistic 3D simulations for nonlinear processes may be too expensive to be carried out with high resolution. In these cases, lower dimensionality simulations might be useful. It is straightforward to derive the 2D counterparts of these distributions; however, one needs to consider a slightly different form of 3.2 and the surface element $\mathrm{d}S$. Alternatively, the recently added quasi-3D module of the `OSIRIS` code [70] could be used to leverage on the cylindrical symmetry of the scattering.

An alternative way of accounting for the laser focusing without resorting to the concept of $a_{0,\mathrm{eff}}$ is the overlap method applied in [49]. The overlap is defined as the product of the electron beam density and the laser pulse field amplitude, and is integrated along the particle's trajectories. This can be used to estimate the radiative losses of the electron beam. Although this method could more consistently include the superposition of a temporal envelope and a spatially varying laser field than our approach, this rarely allows for simple explicit analytical formulas, nor is it compatible with scaling laws that already include effects of a temporal envelope.

3.8 Conclusions

In this chapter we have derived distributions of particles in the normalized vector potential of the laser $a_{0,\mathrm{eff}}$ for several geometries of the electron beam, namely for Short, Thin and Wide beams. We have also applied this method to estimate the total number of positrons produced in the scatterings, which prove to be consistent with full PIC-QED simulations.

Here we present a list of some advantages and disadvantages of the method developed here.

- Advantages: Allows global computations of observables, starting from Plane Wave scaling laws. Histograms are additive, so if one can describe the effect of two laser scalar fields separately, it is possible in principle to describe their combined effect (if interference effects of the fields can be neglected).

- Disadvantages: Requires some calculation effort before obtaining the approximate distributions. Not practical if one only needs to calculate few momenta of the local scalar function or if the density $n(\vec{r})$ or scalar function $a(\vec{r})$ are very oscillatory/non-injective. Even with access to the analytical particle distribution, the full calculation of the global yield might not be feasible analytically, and one is forced to use numerical methods.

The method detailed in this chapter (see equation 3.4) is mathematically very similar (although more general) to the Density-of-States calculations in Condensed Matter Physics. Further analogies between the two subjects have not been explored.

Chapter 4

Optimal focusing strategy to obtain the maximum positron yield

4.1 Introduction

Having proved in the last chapter the consistency of the $a_{0,\mathrm{eff}}$ approach, we now address the issue of the optimal focusing strategy for a wide range of laser parameters (in particular as a function of total energy content and pulse duration), as well as different electron beam energies. For the remainder of this chapter we assume that the electron beam is of a Wide geometry, with 200 μm long (flat-top longitudinal envelope) and has a Gaussian transverse beam profile with $\sigma_x = 24.4\ \mu\mathrm{m}$ and $\sigma_y = 29.6\ \mu\mathrm{m}$, an on-axis beam density $n_b = 10^{16}\ \mathrm{cm}^{-3}$ corresponding to a total beam charge of $Q_b = 2\ \mathrm{nC}$, and results can be rescaled to other values for the central beam density by introducing a factor $n_b/10^{16}\ \mathrm{cm}^{-3}$. The electron beam is spatio-temporally synchronized with the laser (i.e., the center of the beam interacts with the laser peak at the focal plane, and they share the propagation axis).

4.2 Varying the laser spotsize

A specific laser system has a fixed total energy content, which for a Gaussian transverse profile is approximately given by $\varepsilon[\mathrm{J}] \sim 2.1 \times 10^{-5}\ \ a_0^2\ (W_0/\lambda)^2\ \tau[\mathrm{fs}]$. The laser intensity (proportional to a_0^2) is therefore inversely proportional to the square of the spot size W_0. As the number of pairs produced per interacting electron N_+^{PW} is a monotonously rising function of the effective a_0, and the number of seed electrons that would experience the high intensity is proportional to the size of the interaction volume $\sim W_0^2\ z_R \sim W_0^4$, to obtain the highest possible number of positrons, one should strike the right balance between a high value of a_0 and a large W_0. In other words, there is a trade-off between using a short focal length to obtain the highest conceivable laser intensity and having a wider interaction volume where more seed electrons participate in the interaction.

What follows is a calculation of the optimal focal spot and the corresponding pair yield for lasers with energy below $1\ \mathrm{kJ}$ and relativistic particle beams with energies lower or equal to $20\ \mathrm{GeV}$. These values include what will soon be available in several experimental facilities (e.g. SLAC [57], HiBEF [82] or ELI [54]). For each combination of the electron beam energy and the laser total energy content, we apply the analytical expression (see Table 3.1) to calculate the effective a_0 distribution of the interacting particles. Then, we integrate the results numerically to find the optimal spotsize and maximum positron yield for this set of parameters (as illustrated in figure 4.1).

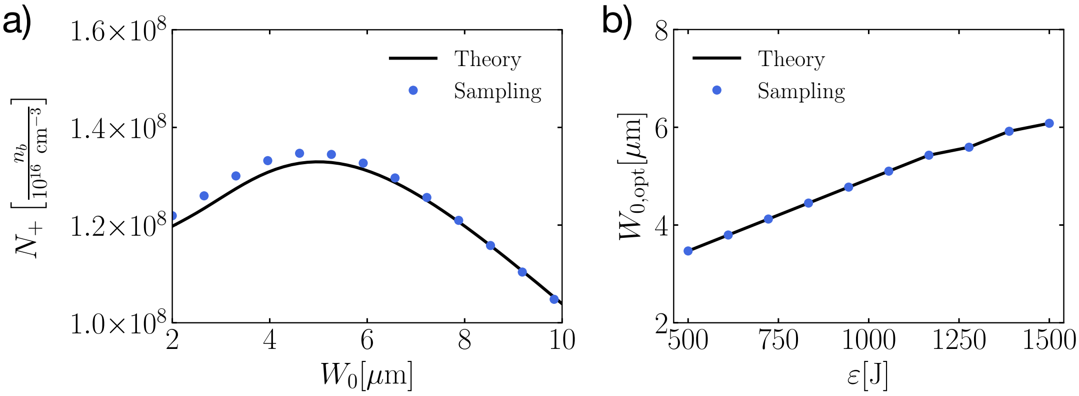

Figure 4.1: a) Positron yield as a function of the laser spot size keeping the total energy contained within the laser pulse constant at $\varepsilon = 1\ \mathrm{kJ}$. b) Optimal spot size for different total laser pulse energies. Beam parameters are $E_0 = 10\ \mathrm{GeV}, L = 200\ \mu\mathrm{m}, \sigma_x = 24.4\ \mu\mathrm{m}, \sigma_y = 29.6\ \mu\mathrm{m}, n_b = 10^{16}\ \mathrm{cm}^{-3}$, and we consider $\tau = 150\ \mathrm{fs}$ with $\lambda = 0.8\ \mu\mathrm{m}$.

4.3 Parameter study for future laser facilities

Figure 4.2 summarizes the optimization results covering ~ 1000 different parameter combinations, keeping the laser duration constant at $35\ \mathrm{fs}$. For 10 GeV electrons and a 1 kJ laser, a maximum number of pairs is 10^9, which is obtained using $W_0 > 8\ \mu\mathrm{m}$. The FACET-II 13 GeV electron beam at SLAC could generate 4×10^8 pairs/shot if paired with a $300\ \mathrm{J}$ laser-focused to $W_0 = 5.7\ \mu\mathrm{m}$. The LUXE $17.5\ \mathrm{GeV}$ beam with the same laser parameters could produce 7×10^8 pairs per shot, using a slightly larger $W_0 = 6.8\ \mu\mathrm{m}$.

Similarly, figure 4.3 shows how to obtain optimal results as a function of the laser energy and the laser pulse duration, keeping the initial electron beam energy constant at $13\ \mathrm{GeV}$. This allows estimating the positron yield at ELI Beamlines, where L4 laser specifications are at $1.5\ \mathrm{kJ}$ with $150\ \mathrm{fs}$ duration. If we assume a third of the laser energy is used to accelerate electrons, $1\ \mathrm{kJ}$ is available for the scattering, which can produce $2.4\times10^8\ (n_b/10^{16}\ \mathrm{cm}^{-3})$ pairs per shot using $W_0 = 6.2\ \mu\mathrm{m}$.

4.4 Effect of longitudinal jitter

As an illustrative example, in figure 4.4 we show the variation in the number of positrons for different values of a_0, for synchronized and an offset of $10\ \mu\mathrm{m}$. In this case, the offset is much smaller than the

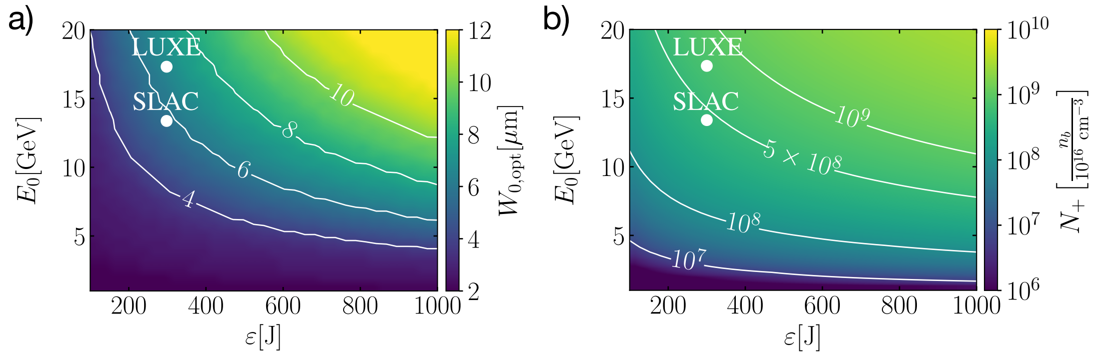

Figure 4.2: Optimization study for lasers pulses of fixed duration ($\tau = 35$ fs). a) Optimal laser spotsize for a head-on scattering as a function of total pulse energy and the electron energy. b) Positron yield achieved using the optimal spotsize. The laser wavelength is $\lambda = 0.8\ \mu\mathrm{m}$; the electron beam is $L = 200\ \mu\mathrm{m}$ long (flat-top longitudinal profile)

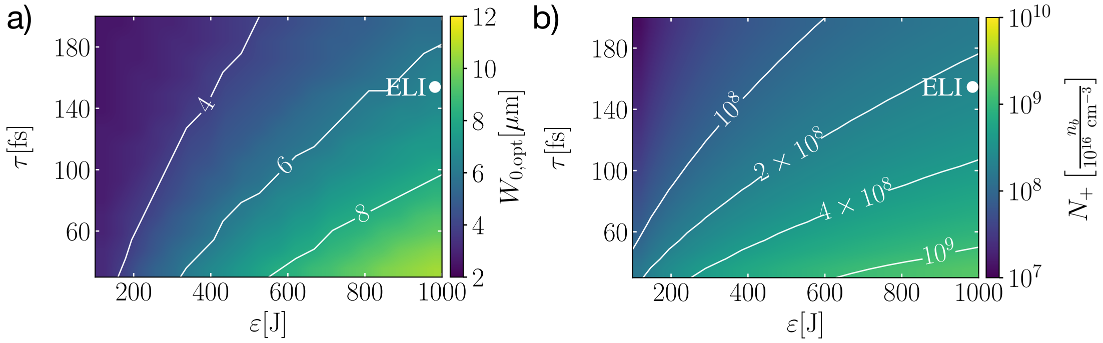

Figure 4.3: Optimization study for fixed electron beam parameters (here, electron energy is 13 GeV, corresponding to an accelerator beam available for example at SLAC). a) Optimal laser spotsize for a head-on scattering as a function of pulse energy and duration. b) Positron yield achieved using the optimal spotsize. Other laser and electron parameters are the same as in figure 4.2

Rayleigh range, which implies a small variation in the final positron yield.

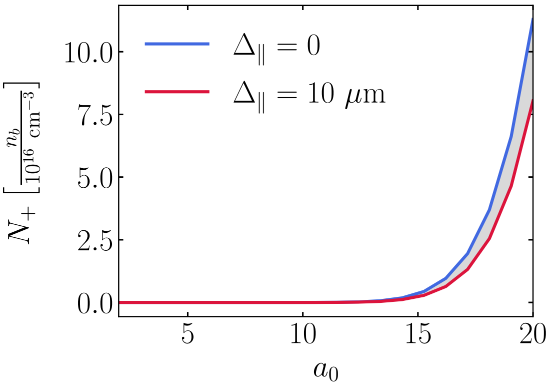

Figure 4.4: Effect of longitudinal jitter of laser on the positron yield. Beam parameters are $E_0 = 3\ \mathrm{GeV}, L = 10\ \mu\mathrm{m}$ and laser parameters $\tau = 30.92\ \mathrm{fs}, \lambda = 0.8\ \mu\mathrm{m}, W_0 = 3\ \mu\mathrm{m}$. The gray area indicates the region for intermediate values of jitter.

The highlighted cases were chosen to reflect the parameters we expect to be available in near-future laser facilities. As time delay and misalignment can be considered, in cases where there are uncertainties about specific experimental parameters, our models can be used as direct support for statistical analysis on pair production. We could incorporate fluctuations in intensity, temporal and spatial synchronization, as well as the fluctuations in electron beam energy distribution, and predict their impact on the final results.

4.5 Conclusions

In this chapter we have applied the $a_{0,\mathrm{eff}}$ approach outlined in the previous chapter to optimize the positron yield when the spot size is a free parameter of the laser system. We have calculated expected values for different near-future laser facilities and exemplified the effect of longitudinal jitter in the positron number.

Chapter 5

Basics of Quantum Computing

In this chapter we overview the basics of Quantum Computing and its notation.

5.1 Introduction

While a classical binary unit (bit) can only take values 0 or 1 at different times, a quantum bit (qubit) can be in a superposition of states $|0\rangle$ and $|1\rangle$,

$$|\psi\rangle = \alpha|0\rangle + \beta|1\rangle$$

with complex coefficients (called amplitudes) $\alpha, \beta \in \mathbb{C}$ and the restriction $|\alpha|^2 + |\beta|^2 = 1$.

Examples of two-state systems include the spin of the electron (spin up and down) and the polarization of a single photon (vertical and horizontal polarization).

Often qubits are multi-state quantum systems where the two states with lowest energy are used most of the time. This superposition does not have any direct analogue in classical digital computers.

Quantum gates are unitary transformations that operate on a set of qubits. In practice, quantum circuits need to be decomposed into a sequence of 1- and 2-qubits gates. In the case of superconducting qubits, these operations are made through the interaction of the qubits with microwave pulses.

A quantum register is a system comprising multiple qubits. Unlike standard classical logic gates, quantum logic gates are reversible, which promises a reduction in power consumption for large scale computations.

The act of measurement on a set of qubits forces the quantum system to arrive at only one of the many states it can be in, with probability of it being in state $|0\rangle$ given by $|\alpha|^2$. Therefore, to fully leverage the new information processing of quantum computers, many qubits and measurements are required. For example, a two-qubit system can be written in the form

$$\begin{aligned}
|\psi\rangle_{AB} &= |\phi\rangle_A \otimes |\varphi\rangle_B \\
&= (\alpha|0\rangle_A + \beta|1\rangle_A) \otimes (\gamma|0\rangle_B + \delta|1\rangle_B)
\end{aligned}$$

$$
\begin{aligned}
&= \alpha\gamma|0\rangle_A|0\rangle_B + \alpha\delta|0\rangle_A|1\rangle_B + \beta\gamma|1\rangle_A|0\rangle_B + \beta\delta|1\rangle_A|1\rangle_B \\
&= \alpha\gamma|00\rangle + \alpha\delta|01\rangle + \beta\gamma|10\rangle + \beta\delta|11\rangle
\end{aligned}
$$

Quantum computers can in principle solve certain classes of problems that no classical computer ever will in a reasonable amount of time or memory.

A standard example of such an algorithm is Grover's algorithm [83], which for an unstructured search reduces the complexity of searching through N items from $O(N)$ to $O(\sqrt{N})$. This quadratic speedup could be useful in optimization problems and machine learning.

A superpolynomial speedup is achieved for example in Shor's algorithm [84], which factorizes a number into prime terms. While in classical computers the best algorithm for a n-digit number would perform worse than $O(e^{n^{1/3}})$, the quantum version has complexity $O(n^3)$.

5.2 Entanglement

A quantum state is said to be separable if and only if:

$$
|\psi\rangle_{\alpha_1 \dots \alpha_n} = |\phi_1\rangle_{\alpha_1} \otimes \dots \otimes |\phi_n\rangle_{\alpha_n}, \quad \exists |\phi_i\rangle
$$

If this equality cannot be satisfied, the state is said to be entangled, for example the Bell state $|\Phi^+\rangle \equiv (|00\rangle + |11\rangle)/\sqrt{2}$. If we measure the leftmost qubit and obtain $|0\rangle$ we immediately know that the rightmost qubit is in the same state $|0\rangle$ (and similarly for $|1\rangle$).

If we change basis to $|+\rangle = (|0\rangle + |1\rangle)/\sqrt{2},\ |-\rangle = (|0\rangle - |1\rangle)/\sqrt{2}$, this Bell state becomes $|\Phi^+\rangle = (|++\rangle + |--\rangle)/\sqrt{2}$, and the correlation between qubit values still remains. This phenomenon has no classical counterpart and will be present regardless of the basis used.

5.3 Bloch sphere

A geometrical representation of single qubit states is the so-called Bloch sphere, which allows an intuitive view of the effects of quantum gates. Any pure quantum state $\alpha|0\rangle + \beta|1\rangle$ will correspond to a point on the surface of a sphere (up to a global phase). For example, in spherical coordinates (see figure 5.1), the state is given by

$$
|\psi\rangle = \cos(\theta/2)|0\rangle + e^{i\varphi}\sin(\theta/2)|1\rangle
$$

The X, Y and Z gates correspond to π rotations around their respective axes. The Hadamard gate is associated with a π rotation around the $\vec{x} + \vec{z}$ axis. Also, $R_x(\phi)$, $R_y(\phi)$ and $R_z(\phi)$ correspond to a counter-clockwise ϕ rotation around the x, y and z axes, respectively.

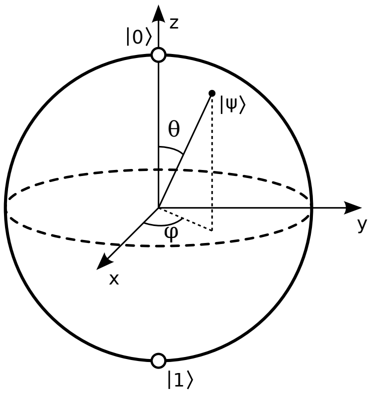

Figure 5.1: Geometrical representation of the state $|\psi\rangle$ of a single qubit using the Bloch sphere.

5.4 Frequently used gates

For reference, in table 5.1 we show a list of frequently used quantum gates with their respective circuit symbols, matrix representation and Dirac notation. As it is clear from the table, using the matrix or Dirac representations will be more or less practical depending on the structure of the operator, namely the number of nonzero entries. For a clear and standard introduction to Quantum Computing, refer to the Nielsen & Chuang textbook [85].

In the next chapter we will apply these concepts for several quantum algorithms.

Name	Symbol	Matrix	Dirac notation
Pauli-X	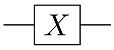	$\begin{bmatrix} 0 & 1 \\ 1 & 0 \end{bmatrix}$	$\|0\rangle\langle 1\| + \|1\rangle\langle 0\|$
Pauli-Y	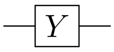	$\begin{bmatrix} 0 & -i \\ i & 0 \end{bmatrix}$	$-i\|0\rangle\langle 1\| + i\|1\rangle\langle 0\|$
Pauli-Z	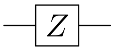	$\begin{bmatrix} 1 & 0 \\ 0 & -1 \end{bmatrix}$	$\|0\rangle\langle 0\| - \|1\rangle\langle 1\|$
Hadamard, H	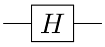	$\frac{1}{\sqrt{2}}\begin{bmatrix} 1 & 1 \\ 1 & -1 \end{bmatrix}$	$\|+\rangle\langle 0\| + \|-\rangle\langle 1\|$
$R_x(\theta) \equiv \exp(-i\theta X/2)$	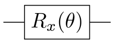	$\begin{bmatrix} \cos(\theta/2) & -i\sin(\theta/2) \\ -i\sin(\theta/2) & \cos(\theta/2) \end{bmatrix}$	$\cos(\theta/2)\|0\rangle\langle 0\| - i\sin(\theta/2)\|0\rangle\langle 1\|$ $-i\sin(\theta/2)\|1\rangle\langle 0\| + \cos(\theta/2)\|1\rangle\langle 1\|$
$R_y(\theta) \equiv \exp(-i\theta Y/2)$	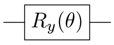	$\begin{bmatrix} \cos(\theta/2) & -\sin(\theta/2) \\ \sin(\theta/2) & \cos(\theta/2) \end{bmatrix}$	$\cos(\theta/2)\|0\rangle\langle 0\| - \sin(\theta/2)\|0\rangle\langle 1\|$ $+\sin(\theta/2)\|1\rangle\langle 0\| + \cos(\theta/2)\|1\rangle\langle 1\|$
$R_z(\theta) \equiv \exp(-i\theta Z/2)$	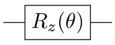	$\begin{bmatrix} 1 & 0 \\ 0 & e^{i\theta} \end{bmatrix}$	$\|0\rangle\langle 0\| + e^{i\phi}\|1\rangle\langle 1\|$
Controlled-NOT, CNOT	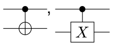	$\begin{bmatrix} 1 & 0 & 0 & 0 \\ 0 & 1 & 0 & 0 \\ 0 & 0 & 0 & 1 \\ 0 & 0 & 1 & 0 \end{bmatrix}$	$\|00\rangle\langle 00\| + \|01\rangle\langle 01\| + \|10\rangle\langle 11\| + \|11\rangle\langle 10\|$
Controlled-U	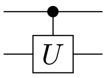	$\begin{bmatrix} 1 & 0 & 0 & 0 \\ 0 & 1 & 0 & 0 \\ 0 & 0 & U_{11} & U_{12} \\ 0 & 0 & U_{21} & U_{22} \end{bmatrix}$	$\|00\rangle\langle 00\| + \|01\rangle\langle 01\|$ $+U_{11}\|10\rangle\langle 10\| + U_{12}\|10\rangle\langle 11\|$ $+U_{21}\|11\rangle\langle 10\| + U_{22}\|11\rangle\langle 11\|$
SWAP	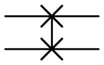	$\begin{bmatrix} 1 & 0 & 0 & 0 \\ 0 & 0 & 1 & 0 \\ 0 & 1 & 0 & 0 \\ 0 & 0 & 0 & 1 \end{bmatrix}$	$\|00\rangle\langle 00\| + \|10\rangle\langle 01\| + \|01\rangle\langle 10\| + \|11\rangle\langle 11\|$

Table 5.1: List of frequently used quantum gates.

Chapter 6

Applications of Quantum Computing

6.1 Introduction

In this chapter, we explore some techniques in quantum computing that may be of use in simulating extreme plasma physics.

This chapter is organized as follows. In section 6.2 we discuss some basic building blocks of Hamiltonian simulation. In section 6.3 we overview linear dynamics techniques, from the standard Vlasov equation to the Fokker-Planck approach, and then the Boltzmann equation. In section 6.4 we discuss the Carleman linearization technique and a simple application. In section 6.5 we review variational algorithms, the new standard for the SWAP test, an example of linear dynamics and the expressibility of variational circuits.

6.2 Building blocks

In this section, we review some basics of Hamiltonian simulations, which have applications beyond the Schrödinger equation.

6.2.1 Standard Hamiltonian

Hamiltonians of the type $Z^{\otimes n}$ are frequent in many areas of Physics, for example, in the transverse-field Hamiltonians of the quantum Ising model. Other tensors of Pauli matrices can be built by applying $X = H^\dagger Z H$ and $Y = -P^\dagger H^\dagger Z H P$, where H is the Hadamard gate (not to be confused with the Hamiltonian) and $P = R_x(\pi/2)$ is the Phase gate. To simulate these Hamiltonians during a time-step Δt, one can use the algorithm by [85], where the parity of each entry in the matrix representation of the unitary operator $U = e^{-i\Delta t H}$ is used to enforce the phase $e^{-i\Delta t Z}$, as shown in figure 6.1. One important characteristic of this algorithm is that its structure does not change with different choices of the time-step, allowing large changes in precision while maintaining its complexity. Furthermore, it only requires one ancilla qubit, a type of qubit which is not used to represent the wavefunction of the physical system of interest, but only to perform intermediary or auxiliary calculations. In practice, usually, not all qubits are connected, so additional intermediate steps are necessary to perform this computation. However, the number of CNOT gates scales approximately linearly with the number of qubits.

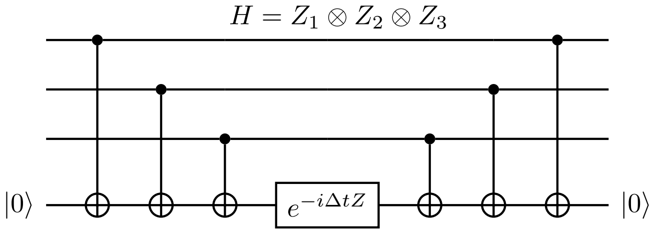

Figure 6.1: Simulation of the Hamiltonian $H = Z^{\otimes 3}$ for an interval Δt.

6.2.2 Linear Schrödinger equation

The linear single-particle Schrödinger equation is the building block for all ideal quantum simulations, as it is the native physical system in a quantum computer.

$$i\hbar \frac{\partial}{\partial t}\psi = H\psi \tag{6.1}$$

The Hamiltonian $H = K + V$ is the sum of a kinetic and a potential term. The potential term varies according to the potential externally imposed.

The implementation of $V(x)$ is straightforward, as this operator is diagonal in the x-basis. To enforce in a systematic way the phases $e^{-iV(x_j)}$ in each entry (j, j) of the matrix representation [86], the procedure in 6.2.1 can be used. However, as the coordinate and momentum operators don't commute ($[x, p] \neq 0$, cannot be diagonalized simultaneously in the same basis), we cannot write the $K(p) = p^2/2m$ operator directly. Instead, we can leverage on the Quantum Fourier Transform (QFT) algorithm, to first apply the $V(x)$ operator in x-basis, then change to p-basis by applying QFT, apply $K(p)$, and finally, undo the transformation by applying the inverse QFT,

$$U = \mathrm{QFT}^{-1}\, e^{-\frac{i}{\hbar}K(p)\epsilon}\, \mathrm{QFT}\, e^{-\frac{i}{\hbar}V(x)\epsilon} \tag{6.2}$$

where ϵ is the time-step, which will determine the accuracy of the simulation. To implement the potential and kinetic terms, each operator needs to be written in binary form

$$k = k_{n-1}2^{n-1} + \cdots + k_1 2 + k_0 \tag{6.3}$$

Then, their representation in terms of gates is

$$\hat{k} = -\sqrt{\frac{1}{2^{2n-3}}\frac{\phi}{\Delta t}}\left(1 + \sum_{j=1}^{n} 2^{n-j}\hat{Z}_j\right) \tag{6.4}$$

and their action over a time-step is

$$\exp\left(-i\hat{k}^2\Delta t\right) = \exp\left(-i\frac{\phi}{2^{2n-3}}\left(1+\sum_{j=1}^{n}2^{n-j}\hat{Z}_j\right)^2\right) \tag{6.5}$$

Any piece-wise polynomial operator similar to this can be written as a product of tensors of Z gates. In the case of a quadratic potential (leading to the simple harmonic oscillator), the implementation of the potential energy unitary operator is straightforward.

In figure 6.2 we show a (classical) simulation of an (initially) Gaussian wavepacket in a quadratic potential, using the same setup as in [86].

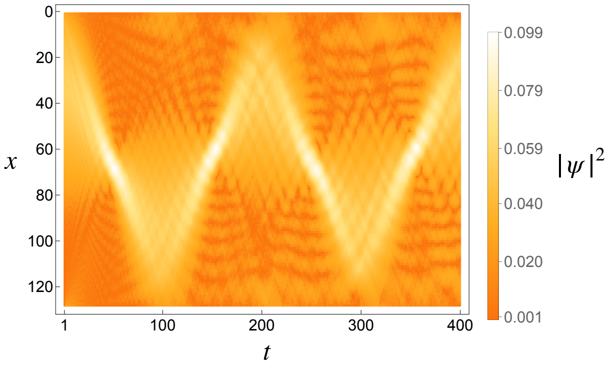

Figure 6.2: Evolution of $|\psi|^2$ for a wavepacket in an harmonic potential.

Increasing quality of quantum hardware has recently allowed for true quantum simulation of the Schrödinger equation. In [87], the author studied the free particle setup with 2 and 3 qubits. More recently, in [88], the author simulated free particle (Gaussian wavepackets and stationary modes), linear and harmonic potentials setups, both for ideal simulation and in an IBM computer. Complementary to this work, [89] studied the free particle, infinite square well, step potential, and quantum tunneling setups.

6.3 Linear dynamics

In this section, we discuss three regimes of plasma dynamics, all of which are linear and therefore directly compatible with standard methods for solving systems of linear equations such as the Harrow-Hassidim-Lloyd (HHL) method [90]. However, this algorithm is not likely to be of use during the NISQ era, as it requires many gates and ancilla qubits for its implementation. Despite this limitation, mapping these physics problems to the quantum paradigm may be beneficial for the design of alternative algorithms.

6.3.1 Linear Vlasov

The Vlasov equation, similarly to the Klimontovich (see equation 2.1) describes the dynamics of a distribution function $f(t,x,v)$ in phase space, where $f(t,x,v)\mathrm{d}^3\vec{x}\mathrm{d}^3\vec{v}$ represents the probability of finding a particle in a volume $\mathrm{d}^3\vec{x}\mathrm{d}^3\vec{v}$.

$$\frac{\mathrm{d}}{\mathrm{d}t}f_s = \frac{\partial f_s}{\partial t} + \mathbf{v}\cdot\boldsymbol{\nabla} f_s + \frac{q}{m}(\mathbf{E}+\mathbf{v}\times\mathbf{B})\cdot\frac{\partial f_s}{\partial \mathbf{v}} = 0 \tag{6.6}$$

The fields $\mathbf{E}, \mathbf{B}$ are either externally imposed or self-consistently evolved in parallel to the distribution function, using Maxwell's equations.

In [91] the authors propose an algorithm to evolve the linearized, electrostatic version of the Vlasov equation. After some approximations, the system of equations becomes

$$\begin{aligned} \frac{\partial \tilde{F}'_j}{\partial t} &= -ik\ v_j\ \tilde{F}'_j - i\alpha_j\ \tilde{E}\ v_j \\ \frac{\partial \tilde{E}}{\partial t} &= -i\sum_j \alpha_j\ \tilde{F}'_j\ v_j \end{aligned} \tag{6.7}$$

Comparison with theory is done through the electric field perturbation $\tilde{E}$, which decays in time as the wave loses energy to the particles in the plasma. The algorithm to evolve the system is the technique of *Qubitization* [92], which, although conceptually intuitive, is also difficult to implement in practice and unlikely to be useful in the NISQ era. The authors claim that their method could be extended to more spatial and momentum dimensions, as well as include more fields and more plasma species.

6.3.2 Fokker-Planck equation

The Fokker-Planck equation is a different approach from the Vlasov equation and is used in areas such as laser-plasma interaction, namely to kinetically model collision between plasma species. An important application is in simulating the energy loss of an electron beam as it interacts with electromagnetic fields [45, 46]. In this case, the particle distribution evolves through

$$\frac{\mathrm{d}}{\mathrm{d}t}f(t,\vec{p}) = \frac{\partial}{\partial p_l}\left[A_l f + \frac{1}{2}\frac{\partial}{\partial p_k}\left(B_{lk} f\right)\right] \tag{6.8}$$

with $A_l = \int q_l w(\vec{p},\vec{q})\mathrm{d}^3\vec{q}, \quad B_{lk} = \int q_l q_k w(\vec{p},\vec{q})\mathrm{d}^3\vec{q}$, the drift and diffusion coefficients respectively, and $w(\vec{p},\vec{q})\ \mathrm{d}^3\vec{p}$ is the probability per unit time of momentum change of the electron $\vec{p}\to\vec{p}-\vec{q}$, with $\vec{q}$ the momentum of the photon.

In [47] the authors apply the Fokker-Planck equation to simulate an electron beam that looses energy as it emits photons. As electrons propagate perpendicularly to a constant magnetic field B, this is effectively a 1D problem. The change in momentum for a single particle then becomes

$$\mathrm{d}\gamma(t) = -S(\chi)\ \mathrm{d}t + \sqrt{R(\chi,\gamma)}\ \mathrm{d}W \tag{6.9}$$

where $S(\chi)$ and $R(\chi,\gamma)$ are related to the QED rate of photon emission, $\chi \propto \gamma\ B$ and $\mathrm{d}W$ is a Wiener motion.

There has been some progress in developing quantum algorithms to solve stochastic differential equations, mainly motivated by finance, physics and biology. In [93] the authors apply a variational method to solve equations of the type

$$\mathrm{d}X(t) = \mu(X(t),t)\ \mathrm{d}t + \sigma(X(t),t)\ \mathrm{d}W \tag{6.10}$$

where $\mu(X(t),t)$ and $\sigma(X(t),t)$ are real-valued functions of time and coordinate, and W is a Brownian motion. This is exactly of the form of equation 6.9.

6.3.3 Plasma-QED Kinetic equations

In the regime where the fraction of the lepton's energy change is close to unity $\mathrm{d}\gamma \leq \gamma$, the Fokker-Planck equation is no longer adequate, and one needs to use the linear Boltzmann equation. Whereas the previous method only connects neighbour grid cells in momentum space, the full Boltzmann equation is dense in the sense that there is a finite probability of a particle transitioning to any other value of energy (as long as physically allowed by conservation laws). The dynamical evolution of lepton-boson distributions functions can be given by [47, 94]

$$\begin{aligned}\frac{\mathrm{d}}{\mathrm{d}t} f_e = &\int_0^{+\infty} w_\chi\left(\gamma+\gamma_\gamma,\gamma_\gamma\right) f_e\left(t,\mathbf{x},\gamma+\gamma_\gamma,\mathbf{\Omega}\right)\ \mathrm{d}\gamma_\gamma \\ &- f_e(t,\mathbf{x},\gamma,\mathbf{\Omega})\int_0^{+\infty} w_\chi\left(\gamma,\gamma_\gamma\right)\ \mathrm{d}\gamma_\gamma\end{aligned} \tag{6.11}$$

$$\frac{\mathrm{d}}{\mathrm{d}t} f_\gamma = \int_1^{+\infty} w_\chi\left(\gamma+\gamma_\gamma,\gamma_\gamma\right) f_e\left(t,\mathbf{x},\gamma+\gamma_\gamma,\mathbf{\Omega}\right)\ \mathrm{d}\gamma \tag{6.12}$$

where $\mathbf{\Omega}$ is the velocity direction and w_χ is the rate of photon emission. Other phenomena such as Pair Production can also be added, which can reduce the photon population and increase the lepton numbers. The RHS of 6.11 is interpreted as a collision term in the Boltzmann equation, while the total time derivative in the LHS is the standard in the Vlasov equation.

An alternative form of these equations is

$$\frac{\mathrm{d}}{\mathrm{d}t}\begin{bmatrix} f_- \\ f_+ \\ f_\gamma \end{bmatrix} = \begin{bmatrix} \mathrm{nCS}_1 & 0 & \mathrm{nBW}_1 \\ 0 & \mathrm{nCS}_1 & \mathrm{nBW}_1 \\ \mathrm{nCS}_2 & \mathrm{nCS}_2 & \mathrm{nBW}_2 \end{bmatrix}\begin{bmatrix} f_- \\ f_+ \\ f_\gamma \end{bmatrix} \tag{6.13}$$

where $f_\pm$ and f_γ are the lepton and photon populations respectively, $\mathrm{nCS}_{1,2}$ and $\mathrm{nBW}_{1,2}$ are submatrices representing the rates of nonlinear Compton Scattering (photon emission) and nonlinear Breit-Wheeler (pair production). A pictorial representation of this matrix can be seen in figure 6.3.

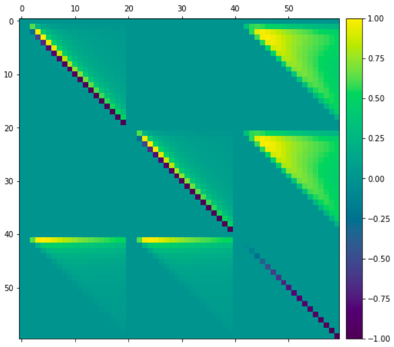

Figure 6.3: Matrix representation of the evolution operator in equation 6.13.

It can be seen that the system is linear in the distribution functions f, and can readily be put into matrix form (although nor Hermitian nor sparse). This problem could then be addressed using HHL [90] (or a variant), but as discussed previously, this approach is not suited for the NISQ era.

6.4 Carleman linearization

6.4.1 Introduction

In [68] the authors apply the Carleman linearization technique to transform a partial differential equation (the Burgers equation) with quadratic nonlinearity into a system of linear differential equations (solvable with HHL). While the original formulation results in an infinite dimension system of equations, for practical applications, the number of equations needs to be truncated at some order N, which will introduce some error. In particular, the method in the paper is able to solve problems of the type:

$$\frac{\mathrm{d}}{\mathrm{d}t}u = F_0(t) + F_1\, u + F_2\, u^{\otimes 2} \tag{6.14}$$

where u is some field over coordinates x (e.g. fluid velocity). The Carleman algorithm scales very quickly in problem size even for small grid resolution, reducing the types of setups one can benchmark in a classical computer. For instance, multidimensional problems with many variables $\mathbf{x}, \mathbf{u}, \mathbf{E}, \mathbf{B}$ and high grid resolution will not possible to simulate classically in a laptop.

6.4.2 Applying Carleman linearization to Kompaneets equation

The Kompaneets equation is a specialized form of the Fokker-Planck equation for a distribution of photons, and contains a diffusion term, a recoil term, and a nonlinear induced emission term. The original version of the equation can only be applied in the nonrelativistic energy regime with the photon energy $h\nu \ll k_B T$ and the electron temperature $k_B T \ll m_e c^2$. This equation has been studied in PIC codes [95]. For a review on the subject, see [96].

The nonlinear Kompaneets equation written for the photon energy distribution function $f = \xi^2 n$, with

n the occupation density, is

$$\frac{\partial}{\partial y} f = 2(\xi - 1)f + \xi^2 \partial_\xi f + 2f\partial_\xi f + \xi^2 \partial_{\xi\xi} f \tag{6.15}$$

where $y = t/t_C$ is the normalized time, and $\xi = \hbar\,\omega/k_B T$ the normalized photon energy. This equation is precisely of the form of 6.14. The quasi-equilibrium solution to 6.15 can be found by equating the right-hand side to zero. This solution leads to a Wien spectrum in the linear case and a Bose-Einstein spectrum in the nonlinear case .

We simulated the Kompaneets equation on a classical computer (by adapting the code of [68]), whose results can be seen in figure 6.4. The initial distribution is a Maxwellian:

$$f(\xi, y = 0) \propto \exp\left(-\frac{(\xi - \langle\xi\rangle)^2}{2\sigma_\xi^2}\right) \tag{6.16}$$

with $\langle\xi\rangle = 0.1$ and $\sigma^2 = \langle\xi^2 - \langle\xi\rangle^2\rangle = 0.1$.

It is clear that using higher order N would result in distributions closer to the Bose-Einstein spectrum. However, this was not done due to the heavy memory requirement of the method.

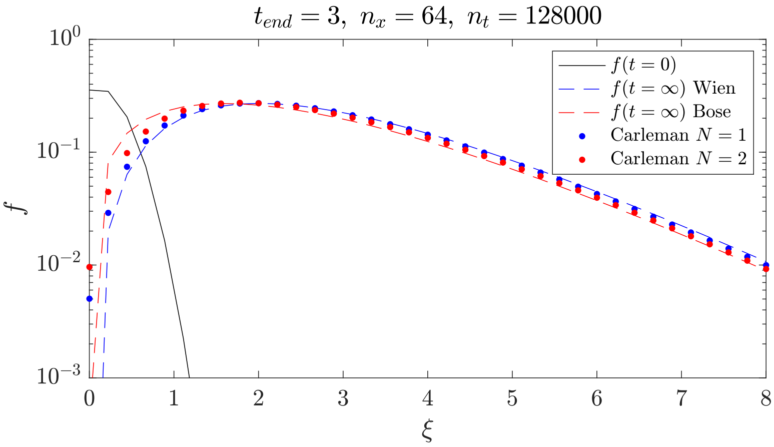

Figure 6.4: Solution of the nonlinear Kompaneets equation using the Carleman linearization technique up to order $N = 2$.

6.5 Variational Quantum Algorithms

6.5.1 Introduction

In the NISQ era it will not be possible to run deep quantum circuits. Direct Hamiltonian simulation (section 6.2.2) is therefore limited to ~ 10 qubits to represent wavefunctions, which is in any case fast to simulate on classical hardware.

Variational algorithms were first developed in the context of quantum chemistry [97] to provide an efficient way of encoding the wavefunction using classical parameters. This has since developed into a subfield of its own, and promises significant advances even in the NISQ era.

This class of algorithms presents some core advantages over direct standard simulation:

- shallower circuits (although perhaps at the expense of doubling the number of qubits), and thus reduced accumulated error
- allows reconstruction of the wavefunction at any time-step (as the wavefunction is described through classical parameters)
- is adaptable to nonlinear dynamics

In variational dynamical evolution, the operator $e^{-iH\Delta t}$ is applied to the wavefunction at time t, described with parameters $\vec{\theta}$, producing $e^{-iH\Delta t}|\psi(t)\rangle$. Another set of parameters $\vec{\theta'}$ will try to approximate the wavefunction at $t+\Delta t$. The quantum computer is used as an efficient calculator of the overlap of the two wavefunctions (how close they are according to some metric), which needs to be measured enough times until some convergence is achieved. The classical machine then applies a minimization routine (e.g. gradient descent) to find the best parameters $\vec{\theta'}$ that describe the wavefunction at the next time-step. The old parameters are stored and updated $\vec{\theta} \leftarrow \vec{\theta'}$. The procedure is repeated until some final time-step. See figure 6.5 for a schematic representation.

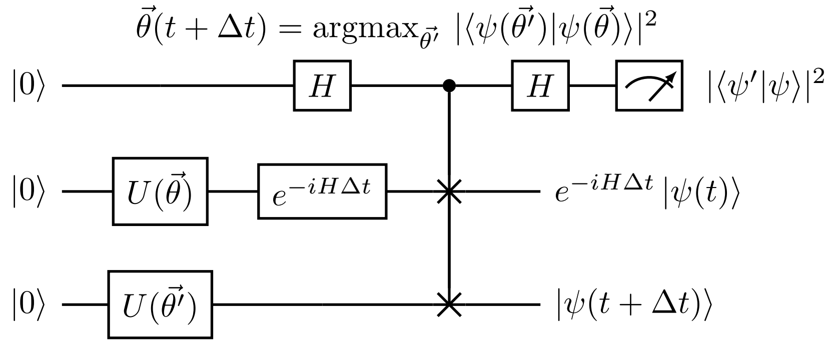
$\vec{\theta}(t+\Delta t) = \mathrm{argmax}_{\vec{\theta'}}\ |\langle\psi(\vec{\theta'})|\psi(\vec{\theta})\rangle|^2$
$|0\rangle$
H
H
$|\langle\psi'|\psi\rangle|^2$
$|0\rangle$
$U(\vec{\theta})$
$e^{-iH\Delta t}$
$e^{-iH\Delta t}\,|\psi(t)\rangle$
$|0\rangle$
$U(\vec{\theta'})$
$|\psi(t+\Delta t)\rangle$

Figure 6.5: Schematic of a variational circuit for dynamical evolution using the original SWAP test. $\vec{\theta}$ and $\vec{\theta'}$ represent the parameters at time t and $t+\Delta t$, respectively.

6.5.2 The SWAP algorithm

The SWAP test [85] is a method that quantifies the overlap between two wave functions ψ and ϕ, and is a very common subroutine in variational algorithms. In [98] the authors applied Machine Learning techniques to arrive at two more efficient versions of the algorithm, called ABA and BBA, with the latter having a constant depth (one layer of parallel CNOT followed by a layer of parallel Hadamards). For wavefunctions $\psi = (|0\rangle + |1\rangle)/\sqrt{2}$ and $\phi = (|0\rangle + e^{i\alpha}|1\rangle)/\sqrt{2}$ (or density states $\rho = |\psi\rangle\langle\psi|$ and $\sigma = |\phi\rangle\langle\phi|$) the overlap will be $|\langle\psi|\phi\rangle|^2 = \cos(\alpha/2)^2$.

We tested the three variations of the algorithm (original, ABA and BBA) on IBM quantum hardware *ibmq_manila* [99]. Results are shown in figure 6.6. As expected, the new BBA algorithm proved closer to the theory than the other approaches near $\alpha \sim 0$ or $\alpha \sim 2\pi$ (which is the region of interest for most variational applications).

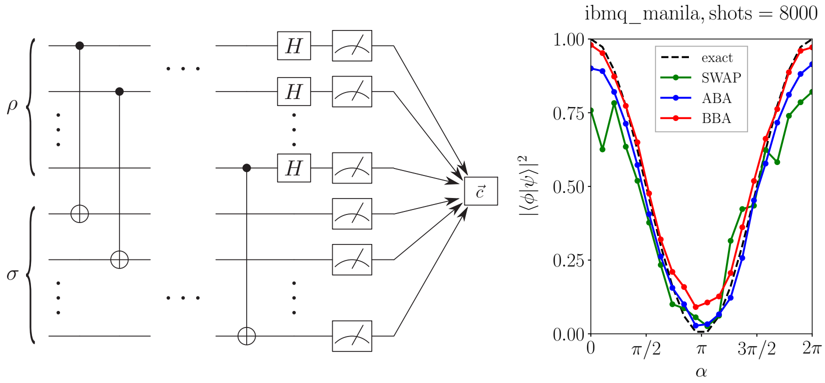

Figure 6.6: Left: schematic of the BBA circuit by Cincio *et al* [98] to measure the overlap between states ρ and σ. Right: simulation results of from a IBM machine *ibmq_manila*.

6.5.3 Simulating cubic gates

Standard quantum gates operate within one or two qubits. However, native cubic gates could be important in areas such as three-wave mixing, a phenomenon that appears in nonlinear optics and turbulence. In [100] the authors discuss the creation of these cubic quantum gates as a way to minimize noise, as their standard counterparts require many quantum operations. In particular, the gate used in the paper to evolve the system during one time-step acts on a *qutrit* (3-level system), while in standard quantum hardware it would be compiled as a gate on 2 qubits ($2\times$ 2-level).

Quantum cloud services (e.g. IBM's [99]) provide compilers that try to minimize the number of quantum gates needed to represent a given operation. We ran the circuit used in [100] on the quantum computer *ibmq_manila*.

In the particular setup of three wave mixing, the evolution operator is periodic (after a number of repetitions it equals the identity). Because of the periodicity of the evolution operator, the compiler recognizes this, and simplifies the necessary sequence of gates. This significantly limits the total error of the circuit (left and middle column of figure 6.7). If running without a compiler, the errors will accumulate rapidly (right column of figure 6.7).

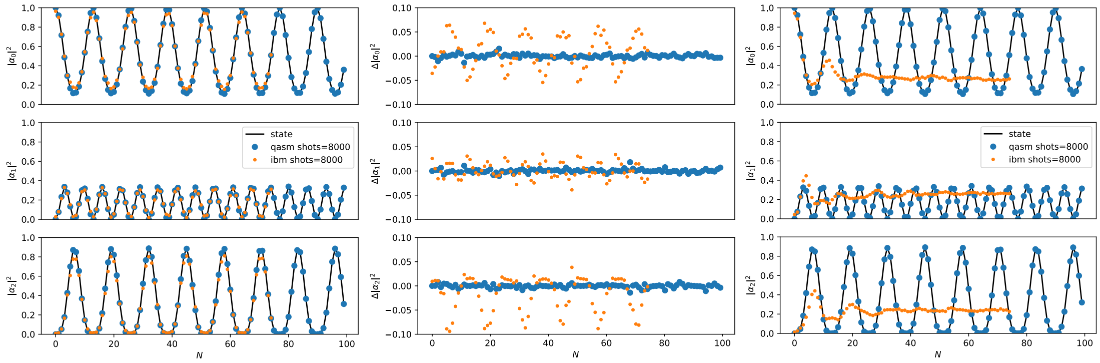

Figure 6.7: Left: compiled circuit. Middle: associated error. Right: Non-compiled circuit. The $|\alpha_i|^2$ correspond to the probabilities of measuring the system in state $|\alpha_i\rangle$.

We also adapted this simulation to be a variational algorithm, which we ran using the previous techniques of section 6.5.1 and the PennyLane API [72] on a classical simulator. To illustrate the importance of a good choice of parameterized circuits, we ran two different *ansätze*, one with 4 parameters and the other with 8. As can be seen in figure 6.8, the former does not capture the dynamics correctly, whereas the latter with 8 parameters does [101].

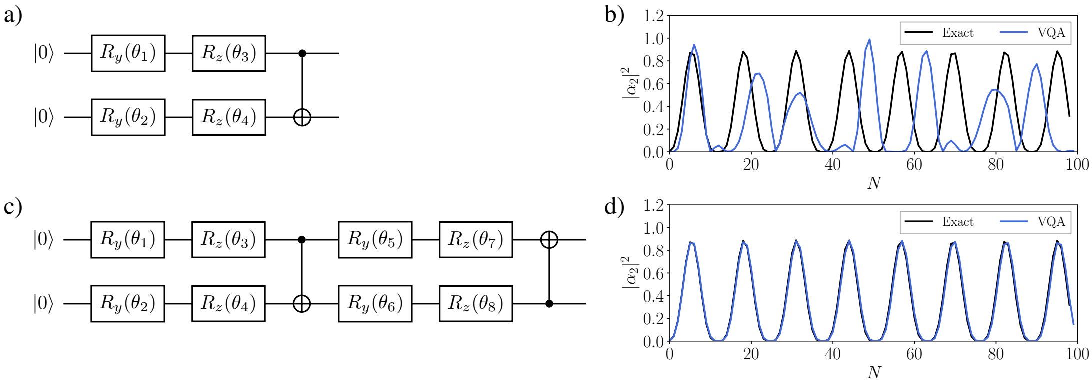

Figure 6.8: Ideal simulation of a variational circuit for the three-wave mixing. a) Circuit of a 1-block ansatz. b) Variational evolution of the $|\alpha_2|^2$ observable with a 1-block ansatz. c) Circuit of a 2-block ansatz and d) respective evolution.

The same logic can be applied to many-qubit systems. However, finding the best ansatz is in itself a computationally intensive task, which has led to the development of physically motivated circuits (e.g. leveraging the symmetries of molecules to simplify the ansatz).

6.6 Conclusions

In this chapter, we reviewed and implemented several quantum simulation techniques (in both real and simulated quantum hardware), with the long-term goal of developing algorithms to study extreme plasmas. Some methods were found more promising than others, especially in the context of applications on near-future quantum computing hardware.

In particular, we simulated the Kompaneets equation using the Carleman technique for the first time and identified potential setups within extreme plasma physics which can be transposed to quantum algorithms.

Chapter 7

Conclusions

7.1 Achievements

In this Thesis, we have defined a new approach to model laser-beam scatterings, through the concept of a distribution in the effective field of the laser $a_{0,\mathrm{eff}}$. This allowed us to make predictions regarding the pair production in laser-electron scattering, taking into account the 3D focusing geometry, spatio-temporal synchronization, and the realistic beam shape and size. This opens a possibility for fast parameter optimization, using analytical calculations directly or combining them with simple numerical integration. The approach is faster than using full-scale Monte Carlo or PIC-QED calculations, and the results can be obtained on a single CPU. Apart from saving computing resources, the ideas from the present study can be applied for real-time optimization and data analysis in experiments.

In summary, the findings of this Thesis are expected to be important for near-future laser-electron scattering experiments, as the calculations are fast and can provide real-time feedback during the course of an experiment.

In the area of Quantum Computing, we have identified several instances of problems in Extreme Plasma Physics which could be addressed using quantum algorithms. Although well established and routinely used in the scientific community, classical multidimensional nonlinear Vlasov codes are very demanding in terms of memory, which hints at the possibility of quantum codes being more efficient for specific applications. Even if it is not efficient to reconstruct entire distribution functions in a quantum computer, momenta like the average and mean-square of distributions can be easily retrieved. It is, therefore, probable that variational algorithms will play an essential role in near-future applications in plasma physics. Our work is a step in this direction.

7.2 Code Contributions

Following the spirit of open science, many of the results presented in this Thesis are available as tutorials and can be found at `https://github.com/OsAmaro/MScThesisRepositories`. In particular, all code written for the chapter on quantum computing is available on the mentioned repository.

7.3 Open Questions and Future Work

One of the major assumptions made in our model is that the beam electrons act as test-particles, that is, they do not influence each other (through Coulomb repulsion) nor the dynamics of the laser pulse. However, if the electron density, laser intensity or collective effects become sufficiently large, this approximation should break down. In particular, for the high χ regime, copious pairs can be created in a cascade-type reaction, and thus deplete the energy of the laser pulse. In principle, this approach could also be applied to beam-beam collisions. However, in this case one should consider the self-consistent evolution of the beam shape, which in some regimes can lead to disruption and thus invalidate the model.

In many instances of the electron-laser scattering, the collision is not perfectly frontal, but at an angle. This is not considered in our work; however, the study of 90º scattering has already begun within the GoLP-EPP group, and it should be possible to obtain the distribution functions for arbitrary collision angles.

So far all particle distributions in $a_{0,\mathrm{eff}}$ were derived in the paraxial approximation. However, for a tightly focused laser $W_0 \sim \lambda$, the wavefront curvatures cannot be neglected and will lower even further the effective field strength due to the non-frontal collision. As the exact field equations for propagation of a tightly-focused Gaussian laser are not available in a simple explicit mathematical form, obtaining explicit particle distributions in this case is a challenging task which we plan to pursue in the future.

Besides Gaussian laser beams, other structured lasers could be considered. For example, in [80] the authors study pair production in Laguerre-Gaussian beams. Even if the complex geometry of these beams would make analytical calculations difficult, the sampling approach could be applied.

Besides optimizing the positron yield considered in this Thesis, the equivalent intensity distributions are going to be useful to calculate the asymptotic energy spread [45–48, 102] and divergence of the interacting electron beams [50, 103–105], which are also imprinted on the emitted photon beams in the hard x-ray and gamma-ray range.

In this work we applied a scaling law for the production of positrons, which is insensitive to the specific spectral shape of the pairs. In future work one could try to apply a more refined model to predict more precisely the energy of the produced pairs, and also other scaling laws (e.g. photon emission, electron energy losses). Other explorations may include the errors associated with: deformation of ballistic trajectories due to ponderomotive force, the breakdown of the LCFA approximation, and the production of more secondary particle generations.

In our future work on quantum algorithms for Extreme Plasma Physics phenomena, the next planned step is to implement the Fokker-Planck algorithm for modelling a radiating electron beam in a constant homogeneous magnetic field, and then iteratively apply the algorithm to more complex and multidimensional field configurations.

Bibliography

[1] J. G. Kirk, A. R. Bell, and I. Arka. Pair production in counter-propagating laser beams. *Plasma Physics and Controlled Fusion*, 51(8):085008, jul 2009. doi: 10.1088/0741-3335/51/8/085008.

[2] D. A. Uzdensky and S. Rightley. Plasma physics of extreme astrophysical environments. *Reports on Progress in Physics*, 77(3):036902, mar 2014. doi: 10.1088/0034-4885/77/3/036902.

[3] A. N. Timokhin. Time-dependent pair cascades in magnetospheres of neutron stars – I. Dynamics of the polar cap cascade with no particle supply from the neutron star surface. *Monthly Notices of the Royal Astronomical Society*, 408(4):2092–2114, 10 2010. ISSN 0035-8711. doi: 10.1111/j.1365-2966.2010.17286.x.

[4] Z. Medin and D. Lai. Pair cascades in the magnetospheres of strongly magnetized neutron stars. *Monthly Notices of the Royal Astronomical Society*, 406(2):1379–1404, 07 2010. ISSN 0035-8711. doi: 10.1111/j.1365-2966.2010.16776.x.

[5] R. D. Blandford and R. L. Znajek. Electromagnetic extraction of energy from Kerr black holes. *Monthly Notices of the Royal Astronomical Society*, 179(3):433–456, 07 1977. ISSN 0035-8711. doi: 10.1093/mnras/179.3.433. URL `https://doi.org/10.1093/mnras/179.3.433`.

[6] K. Parfrey, A. Philippov, and B. Cerutti. First-principles plasma simulations of black-hole jet launching. *Phys. Rev. Lett.*, 122:035101, Jan 2019. doi: 10.1103/PhysRevLett.122.035101. URL `https://link.aps.org/doi/10.1103/PhysRevLett.122.035101`.

[7] V. I. Ritus. Quantum effects of the interaction of elementary particles with an intense electromagnetic field. *Journal of Soviet Laser Research*, 6:497617, Sep 1985. doi: 10.1007/BF01120220.

[8] T. Erber. High-energy electromagnetic conversion processes in intense magnetic fields. *Rev. Mod. Phys.*, 38:626–659, Oct 1966. doi: 10.1103/RevModPhys.38.626.

[9] J. S. Toll. The Dispersion relation for light and its application to problems involving electron pairs. Thesis, 1952.

[10] G. A. Mourou, T. Tajima, and S. V. Bulanov. Optics in the relativistic regime. *Rev. Mod. Phys.*, 78: 309–371, Apr 2006. doi: 10.1103/RevModPhys.78.309. URL `https://link.aps.org/doi/10.1103/RevModPhys.78.309`.

[11] M. Marklund and P. K. Shukla. Nonlinear collective effects in photon-photon and photon-plasma interactions. *Rev. Mod. Phys.*, 78:591–640, May 2006. doi: 10.1103/RevModPhys.78.591. URL `https://link.aps.org/doi/10.1103/RevModPhys.78.591`.

[12] A. Di Piazza, C. Müller, K. Z. Hatsagortsyan, and C. H. Keitel. Extremely high-intensity laser interactions with fundamental quantum systems. *Rev. Mod. Phys.*, 84:1177–1228, Aug 2012. doi: 10.1103/RevModPhys.84.1177. URL `https://link.aps.org/doi/10.1103/RevModPhys.84.1177`.

[13] A. Di Piazza, K. Z. Hatsagortsyan, and C. H. Keitel. Harmonic generation from laser-driven vacuum. *Phys. Rev. D*, 72:085005, Oct 2005. doi: 10.1103/PhysRevD.72.085005. URL `https://link.aps.org/doi/10.1103/PhysRevD.72.085005`.

[14] A. Fedotov and N. Narozhny. Generation of harmonics by a focused laser beam in the vacuum. *Physics Letters A*, 362(1):1–5, 2007. ISSN 0375-9601. doi: https://doi.org/10.1016/j.physleta.2006.09.085. URL `https://www.sciencedirect.com/science/article/pii/S0375960106015271`.

[15] T. Heinzl, B. Liesfeld, K.-U. Amthor, H. Schwoerer, R. Sauerbrey, and A. Wipf. On the observation of vacuum birefringence. *Optics Communications*, 267(2):318–321, 2006. ISSN 0030-4018. doi: https://doi.org/10.1016/j.optcom.2006.06.053. URL `https://www.sciencedirect.com/science/article/pii/S0030401806006481`.

[16] B. King, P. Böhl, and H. Ruhl. Vacuum high-harmonic generation in the shock regime and photon-photon scattering dynamics. *Journal of Physics: Conference Series*, 691:012022, feb 2016. doi: 10.1088/1742-6596/691/1/012022. URL `https://doi.org/10.1088/1742-6596/691/1/012022`.

[17] T. Grismayer, M. Vranic, J. L. Martins, R. A. Fonseca, and L. O. Silva. Laser absorption via quantum electrodynamics cascades in counter propagating laser pulses. *Physics of Plasmas*, 23(5):056706, 2016. doi: 10.1063/1.4950841.

[18] W. Luo, W.-Y. Liu, T. Yuan, M. Chen, J.-Y. Yu, F.-Y. Li, D. Del Sorbo, C. P. Ridgers, and Z.-M. Sheng. Qed cascade saturation in extreme high fields. *Scientific Reports*, 8(1):8400, May 2018. ISSN 2045-2322. doi: 10.1038/s41598-018-26785-8.

[19] N. V. Elkina, A. M. Fedotov, I. Y. Kostyukov, M. V. Legkov, N. B. Narozhny, E. N. Nerush, and H. Ruhl. Qed cascades induced by circularly polarized laser fields. *Phys. Rev. ST Accel. Beams*, 14:054401, May 2011. doi: 10.1103/PhysRevSTAB.14.054401.

[20] K. Qu, S. Meuren, and N. J. Fisch. Signature of collective plasma effects in beam-driven qed cascades, 2020. URL `https://arxiv.org/abs/2001.02590`.

[21] S. S. Bulanov, C. B. Schroeder, E. Esarey, and W. P. Leemans. Electromagnetic cascade in high-energy electron, positron, and photon interactions with intense laser pulses. *Phys. Rev. A*, 87:062110, Jun 2013. doi: 10.1103/PhysRevA.87.062110.

[22] A. R. Bell and J. G. Kirk. Possibility of prolific pair production with high-power lasers. *Phys. Rev. Lett.*, 101:200403, Nov 2008. doi: 10.1103/PhysRevLett.101.200403.

[23] S. S. Bulanov, N. B. Narozhny, V. D. Mur, and V. S. Popov. Electron-positron pair production by electromagnetic pulses. *Journal of Experimental and Theoretical Physics*, 102(1):9–23, Jan 2006. ISSN 1090-6509. doi: 10.1134/S106377610601002X.

[24] E. N. Nerush, I. Y. Kostyukov, A. M. Fedotov, N. B. Narozhny, N. V. Elkina, and H. Ruhl. Laser field absorption in self-generated electron-positron pair plasma. *Phys. Rev. Lett.*, 106:035001, Jan 2011. doi: 10.1103/PhysRevLett.106.035001.

[25] A. A. Mironov, A. M. Fedotov, and N. B. Narozhnyi. Generation of quantum-electrodynamic cascades in oblique collisions of ultrarelativistic electrons with an intense laser field. *Quantum Electronics*, 46(4):305–309, apr 2016. doi: 10.1070/qel16057.

[26] M. Lobet, E. d'Humières, M. Grech, C. Ruyer, X. Davoine, and L. Gremillet. Modeling of radiative and quantum electrodynamics effects in PIC simulations of ultra-relativistic laser-plasma interaction. *Journal of Physics: Conference Series*, 688:012058, mar 2016. doi: 10.1088/1742-6596/688/1/012058.

[27] M. Vranic, T. Grismayer, J. Martins, R. Fonseca, and L. Silva. Particle merging algorithm for pic codes. *Computer Physics Communications*, 191:65–73, 2015. ISSN 0010-4655. doi: https://doi.org/10.1016/j.cpc.2015.01.020.

[28] R. Duclous, J. G. Kirk, and A. R. Bell. Monte carlo calculations of pair production in high-intensity laser–plasma interactions. *Plasma Physics and Controlled Fusion*, 53(1):015009, nov 2010. doi: 10.1088/0741-3335/53/1/015009. URL `https://doi.org/10.1088/0741-3335/53/1/015009`.

[29] A. Gonoskov, S. Bastrakov, E. Efimenko, A. Ilderton, M. Marklund, I. Meyerov, A. Muraviev, A. Sergeev, I. Surmin, and E. Wallin. Extended particle-in-cell schemes for physics in ultrastrong laser fields: Review and developments. *Phys. Rev. E*, 92:023305, Aug 2015. doi: 10.1103/PhysRevE.92.023305.

[30] V. F. Bashmakov, E. N. Nerush, I. Y. Kostyukov, A. M. Fedotov, and N. B. Narozhny. Effect of laser polarization on quantum electrodynamical cascading. *Physics of Plasmas*, 21(1):013105, 2014. doi: 10.1063/1.4861863.

[31] E. G. Gelfer, A. A. Mironov, A. M. Fedotov, V. F. Bashmakov, E. N. Nerush, I. Y. Kostyukov, and N. B. Narozhny. Optimized multibeam configuration for observation of qed cascades. *Phys. Rev. A*, 92:022113, Aug 2015. doi: 10.1103/PhysRevA.92.022113.

[32] M. Vranic, T. Grismayer, R. A. Fonseca, and L. O. Silva. Electron–positron cascades in multiple-laser optical traps. *Plasma Physics and Controlled Fusion*, 59(1):014040, nov 2016. doi: 10.1088/0741-3335/59/1/014040.

[33] A. Gonoskov, A. Bashinov, S. Bastrakov, E. Efimenko, A. Ilderton, A. Kim, M. Marklund, I. Meyerov, A. Muraviev, and A. Sergeev. Ultrabright gev photon source via controlled electromagnetic cascades in laser-dipole waves. *Phys. Rev. X*, 7:041003, Oct 2017. doi: 10.1103/PhysRevX.7.041003.

[34] M. Jirka, O. Klimo, S. V. Bulanov, T. Z. Esirkepov, E. Gelfer, S. S. Bulanov, S. Weber, and G. Korn. Electron dynamics and γ and e^-e^+ production by colliding laser pulses. *Phys. Rev. E*, 93:023207, Feb 2016. doi: 10.1103/PhysRevE.93.023207.

[35] T. Grismayer, M. Vranic, J. L. Martins, R. A. Fonseca, and L. O. Silva. Seeded qed cascades in counterpropagating laser pulses. *Phys. Rev. E*, 95:023210, Feb 2017. doi: 10.1103/PhysRevE.95.023210.

[36] I. Y. Kostyukov and E. N. Nerush. Production and dynamics of positrons in ultrahigh intensity laser-foil interactions. *Physics of Plasmas*, 23(9):093119, 2016. doi: 10.1063/1.4962567.

[37] M. Jirka, O. Klimo, M. Vranic, S. Weber, and G. Korn. Qed cascade with 10 pw-class lasers. *Scientific Reports*, 7(1):15302, Nov 2017. ISSN 2045-2322. doi: 10.1038/s41598-017-15747-1.

[38] J. W. Yoon, Y. G. Kim, I. W. Choi, J. H. Sung, H. W. Lee, S. K. Lee, and C. H. Nam. Realization of laser intensity over 10^{23} w/cm2. *Optica*, 8(5):630–635, May 2021. doi: 10.1364/OPTICA.420520. URL `http://www.osapublishing.org/optica/abstract.cfm?URI=optica-8-5-630`.

[39] F. Albert, M. E. Couprie, A. Debus, M. C. Downer, J. Faure, A. Flacco, L. A. Gizzi, T. Grismayer, A. Huebl, C. Joshi, M. Labat, W. P. Leemans, A. R. Maier, S. P. D. Mangles, P. Mason, F. Mathieu, P. Muggli, M. Nishiuchi, J. Osterhoff, P. P. Rajeev, U. Schramm, J. Schreiber, A. G. R. Thomas, J.-L. Vay, M. Vranic, and K. Zeil. 2020 roadmap on plasma accelerators. *New Journal of Physics*, 23(3):031101, mar 2021. doi: 10.1088/1367-2630/abcc62. URL `https://doi.org/10.1088/1367-2630/abcc62`.

[40] X.-L. Zhu, T.-P. Yu, Z.-M. Sheng, Y. Yin, I. C. E. Turcu, and A. Pukhov. Dense gev electron–positron pairs generated by lasers in near-critical-density plasmas. *Nature Communications*, 7(1):13686, Dec 2016. ISSN 2041-1723. doi: 10.1038/ncomms13686. URL `https://doi.org/10.1038/ncomms13686`.

[41] X.-L. Zhu, T.-P. Yu, M. Chen, S.-M. Weng, and Z.-M. Sheng. Generation of GeV positron and γ-photon beams with controllable angular momentum by intense lasers. *New Journal of Physics*, 20(8):083013, aug 2018. doi: 10.1088/1367-2630/aad71a. URL `https://doi.org/10.1088/1367-2630/aad71a`.

[42] D. Strickland and G. Mourou. Compression of amplified chirped optical pulses. *Optics Communications*, 56(3):219–221, 1985. ISSN 0030-4018. doi: https://doi.org/10.1016/0030-4018(85)90120-8. URL `https://www.sciencedirect.com/science/article/pii/0030401885901208`.

[43] F. Niel. Classical and quantum description of plasma and radiation in strong fields, 2021. URL `https://www.springer.com/gp/book/9783030735463`.

[44] E. Esarey, C. B. Schroeder, and W. P. Leemans. Physics of laser-driven plasma-based electron accelerators. *Rev. Mod. Phys.*, 81:1229–1285, Aug 2009. doi: 10.1103/RevModPhys.81.1229.

[45] N. Neitz and A. Di Piazza. Stochasticity effects in quantum radiation reaction. *Phys. Rev. Lett.*, 111:054802, Aug 2013. doi: 10.1103/PhysRevLett.111.054802.

[46] M. Vranic, T. Grismayer, R. A. Fonseca, and L. O. Silva. Quantum radiation reaction in head-on laser-electron beam interaction. *New Journal of Physics*, 18(7):073035, jul 2016. doi: 10.1088/1367-2630/18/7/073035.

[47] F. Niel, C. Riconda, F. Amiranoff, R. Duclous, and M. Grech. From quantum to classical modeling of radiation reaction: A focus on stochasticity effects. *Phys. Rev. E*, 97:043209, Apr 2018. doi: 10.1103/PhysRevE.97.043209.

[48] C. P. Ridgers, T. G. Blackburn, D. Del Sorbo, L. E. Bradley, C. Slade-Lowther, C. D. Baird, S. P. D. Mangles, P. McKenna, M. Marklund, C. D. Murphy, and et al. Signatures of quantum effects on radiation reaction in laser–electron-beam collisions. *Journal of Plasma Physics*, 83(5):715830502, 2017. doi: 10.1017/S0022377817000642.

[49] T. Blackburn. Measuring quantum radiation reaction in laser-electron-beam collisions. *Plasma Physics and Controlled Fusion*, 57, 05 2015. doi: 10.1088/0741-3335/57/7/075012.

[50] M. Tamburini. On-shot diagnostic of electron beam-laser pulse interaction based on stochastic quantum radiation reaction, 2020. URL `https://arxiv.org/abs/2007.02841`.

[51] T. G. Blackburn, E. Gerstmayr, S. P. D. Mangles, and M. Marklund. Model-independent inference of laser intensity. *Phys. Rev. Accel. Beams*, 23:064001, Jun 2020. doi: 10.1103/PhysRevAccelBeams.23.064001.

[52] J. M. Cole, K. T. Behm, E. Gerstmayr, T. G. Blackburn, J. C. Wood, C. D. Baird, M. J. Duff, C. Harvey, A. Ilderton, and A. S. e. a. Joglekar. Experimental evidence of radiation reaction in the collision of a high-intensity laser pulse with a laser-wakefield accelerated electron beam. *Phys. Rev. X*, 8:011020, Feb 2018. doi: 10.1103/PhysRevX.8.011020.

[53] K. Poder, M. Tamburini, G. Sarri, A. Di Piazza, S. Kuschel, C. D. Baird, K. Behm, S. Bohlen, J. M. Cole, and D. J. e. a. Corvan. Experimental signatures of the quantum nature of radiation reaction in the field of an ultraintense laser. *Phys. Rev. X*, 8:031004, Jul 2018. doi: 10.1103/PhysRevX.8.031004.

[54] Eli science and technology with ultra-intense lasers whitebook, edited by andreas thoss (2011).

[55] Apollon. URL `http://www.apollon-laser.fr/`.

[56] Corels. URL `https://corels.ibs.re.kr/html/corels_en/`.

[57] Facet-ii. URL `https://portal.slac.stanford.edu/sites/ard_public/facet/Pages/FACET-II.aspx`.

[58] S. Meuren, P. H. Bucksbaum, N. J. Fisch, F. Fiúza, S. Glenzer, M. J. Hogan, K. Qu, D. A. Reis, G. White, and V. Yakimenko. On seminal hedp research opportunities enabled by colocating multi-petawatt laser with high-density electron beams, 2020. URL `https://arxiv.org/abs/2002.10051`.

[59] H. Abramowicz, M. Altarelli, R. Aßmann, T. Behnke, Y. Benhammou, O. Borysov, M. Borysova, R. Brinkmann, F. Burkart, and K. B. et al. Letter of intent for the luxe experiment, 2019. URL `https://arxiv.org/abs/1909.00860`.

[60] Excels. URL `http://www.xcels.iapras.ru`.

[61] Zeus. URL `https://zeus.engin.umich.edu`.

[62] R. P. Feynman. Simulating physics with computers. *International Journal of Theoretical Physics*, 21(6):467–488, Jun 1982. ISSN 1572-9575. doi: 10.1007/BF02650179. URL `https://doi.org/10.1007/BF02650179`.

[63] F. Arute, K. Arya, R. Babbush, D. Bacon, J. C. Bardin, R. Barends, R. Biswas, S. Boixo, F. G. S. L. Brandao, D. A. Buell, B. Burkett, Y. Chen, Z. Chen, B. Chiaro, R. Collins, W. Courtney, A. Dunsworth, E. Farhi, B. Foxen, A. Fowler, C. Gidney, M. Giustina, R. Graff, K. Guerin, S. Habegger, M. P. Harrigan, M. J. Hartmann, A. Ho, M. Hoffmann, T. Huang, T. S. Humble, S. V. Isakov, E. Jeffrey, Z. Jiang, D. Kafri, K. Kechedzhi, J. Kelly, P. V. Klimov, S. Knysh, A. Korotkov, F. Kostritsa, D. Landhuis, M. Lindmark, E. Lucero, D. Lyakh, S. Mandrà, J. R. McClean, M. McEwen, A. Megrant, X. Mi, K. Michielsen, M. Mohseni, J. Mutus, O. Naaman, M. Neeley, C. Neill, M. Y. Niu, E. Ostby, A. Petukhov, J. C. Platt, C. Quintana, E. G. Rieffel, P. Roushan, N. C. Rubin, D. Sank, K. J. Satzinger, V. Smelyanskiy, K. J. Sung, M. D. Trevithick, A. Vainsencher, B. Villalonga, T. White, Z. J. Yao, P. Yeh, A. Zalcman, H. Neven, and J. M. Martinis. Quantum supremacy using a programmable superconducting processor. *Nature*, 574(7779):505–510, Oct 2019. ISSN 1476-4687. doi: 10.1038/s41586-019-1666-5. URL `https://doi.org/10.1038/s41586-019-1666-5`.

[64] J. Preskill. Quantum Computing in the NISQ era and beyond. *Quantum*, 2:79, Aug. 2018. ISSN 2521-327X. doi: 10.22331/q-2018-08-06-79. URL `https://doi.org/10.22331/q-2018-08-06-79`.

[65] U. D. of Energy. Fusion energy sciences roundtable on quantum information science, 2018. URL `https://science.osti.gov/-/media/fes/pdf/workshop-reports/FES-QIS_report_final-2018-Sept14.pdf`.

[66] A. Engel, G. Smith, and S. E. Parker. Linear embedding of nonlinear dynamical systems and prospects for efficient quantum algorithms. *Physics of Plasmas*, 28(6):062305, 2021. doi: 10.1063/5.0040313. URL `https://doi.org/10.1063/5.0040313`.

[67] I. Y. Dodin and E. A. Startsev. On applications of quantum computing to plasma simulations, 2020. URL `https://arxiv.org/abs/2005.14369`.

[68] J.-P. Liu, H. Øie Kolden, H. K. Krovi, N. F. Loureiro, K. Trivisa, and A. M. Childs. Efficient quantum algorithm for dissipative nonlinear differential equations, 2020. URL `https://arxiv.org/abs/2011.03185`. URL: `https://github.com/hermankolden/CarlemanBurgers`.

[69] S. Lloyd, G. D. Palma, C. Gokler, B. Kiani, Z.-W. Liu, M. Marvian, F. Tennie, and T. Palmer. Quantum algorithm for nonlinear differential equations, 2020. URL `https://arxiv.org/abs/2011.06571`.

[70] R. A. Fonseca, L. O. Silva, F. S. Tsung, V. K. Decyk, W. Lu, C. Ren, W. B. Mori, S. Deng, S. Lee, and T. e. a. Katsouleas. Osiris: A three-dimensional, fully relativistic particle in cell code for modeling plasma based accelerators. In P. M. A. Sloot, A. G. Hoekstra, C. J. K. Tan, and J. J. Dongarra, editors, *Computational Science — ICCS 2002*, pages 342–351, Berlin, Heidelberg, 2002. Springer Berlin Heidelberg. ISBN 978-3-540-47789-1.

[71] IBM. Quantum information software kit (qiskit). URL: `https://github.com/Qiskit`.

[72] V. Bergholm, J. Izaac, M. Schuld, C. Gogolin, M. S. Alam, S. Ahmed, J. M. Arrazola, C. Blank, A. Delgado, S. Jahangiri, K. McKiernan, J. J. Meyer, Z. Niu, A. Száva, and N. Killoran. Pennylane: Automatic differentiation of hybrid quantum-classical computations, 2020. URL `https://arxiv.org/abs/1811.04968`.

[73] O. L. Amaro and M. Vranic. Optimal laser focusing for positron production in laser-electron scattering. *New Journal of Physics*, 2021. URL `http://iopscience.iop.org/article/10.1088/1367-2630/ac2e83`.

[74] L. Landau. *The Classical Theory of Fields*. COURSE OF THEORETICAL PHYSICS. Elsevier Science, 2013. ISBN 9781483293288.

[75] A. Di Piazza, K. Z. Hatsagortsyan, and C. H. Keitel. Quantum radiation reaction effects in multiphoton compton scattering. *Phys. Rev. Lett.*, 105:220403, Nov 2010. doi: 10.1103/PhysRevLett.105.220403.

[76] J. Schwinger. On gauge invariance and vacuum polarization. *Phys. Rev.*, 82:664–679, Jun 1951. doi: 10.1103/PhysRev.82.664.

[77] G. Breit and J. A. Wheeler. Collision of two light quanta. *Phys. Rev.*, 46:1087–1091, Dec 1934. doi: 10.1103/PhysRev.46.1087.

[78] T. G. Blackburn, A. Ilderton, C. D. Murphy, and M. Marklund. Scaling laws for positron production in laser–electron-beam collisions. *Phys. Rev. A*, 96:022128, Aug 2017. doi: 10.1103/PhysRevA.96.022128.

[79] V. N. Baier, V. M. Katkov, and V. M. Strakhovenko. *Electromagnetic Processes at High Energies in Oriented Single Crystals*. WORLD SCIENTIFIC, 1998. doi: 10.1142/2216. URL `https://www.worldscientific.com/doi/abs/10.1142/2216`.

[80] A. Mercuri-Baron, M. Grech, F. Niel, A. Grassi, M. Lobet, A. D. Piazza, and C. Riconda. Impact of the laser spatio-temporal shape on breit–wheeler pair production. *New Journal of Physics*, 23(8):085006, aug 2021. doi: 10.1088/1367-2630/ac1975. URL `https://doi.org/10.1088/1367-2630/ac1975`.

[81] V. Yakimenko, L. Alsberg, E. Bong, G. Bouchard, C. Clarke, C. Emma, S. Green, C. Hast, M. J. Hogan, J. Seabury, N. Lipkowitz, B. O'Shea, D. Storey, G. White, and G. Yocky. Facet-ii facility for advanced accelerator experimental tests. *Phys. Rev. Accel. Beams*, 22:101301, Oct 2019. doi: 10.1103/PhysRevAccelBeams.22.101301.

[82] H. Abramowicz, U. H. Acosta, M. Altarelli, R. Assmann, Z. Bai, T. Behnke, Y. Benhammou, T. Blackburn, S. Boogert, and O. B. et al. Conceptual design report for the luxe experiment, 2021. URL `https://arxiv.org/abs/2102.02032`.

[83] L. K. Grover. A fast quantum mechanical algorithm for database search. In *Proceedings of the Twenty-Eighth Annual ACM Symposium on Theory of Computing*, STOC '96, page 212–219, New York, NY, USA, 1996. Association for Computing Machinery. ISBN 0897917855. doi: 10.1145/237814.237866. URL `https://doi.org/10.1145/237814.237866`.

[84] P. Shor. Algorithms for quantum computation: discrete logarithms and factoring. In *Proceedings 35th Annual Symposium on Foundations of Computer Science*, pages 124–134, 1994. doi: 10.1109/SFCS.1994.365700.

[85] M. A. Nielsen and I. L. Chuang. *Quantum Computation and Quantum Information: 10th Anniversary Edition*. Cambridge University Press, 2010. doi: 10.1017/CBO9780511976667.

[86] G. Benenti and G. Strini. Quantum simulation of the single-particle schrödinger equation. *American Journal of Physics*, 76(7):657–662, Jul 2008. ISSN 1943-2909. doi: 10.1119/1.2894532. URL `http://dx.doi.org/10.1119/1.2894532`.

[87] A. M. F. Rodrigues. Validation of quantum simulations: assessing efficiency and reliability in experimental implementations, 2018. URL `http://hdl.handle.net/1822/59739`.

[88] M. Eltohfa. Quantum simulation of schrödinger's equation, 2021. URL `https://fount.aucegypt.edu/capstone/23`.

[89] M. Abouelela. Quantum simulation of the schrodinger equation using ibm's quantum computers, 2020. URL `https://fount.aucegypt.edu/capstone/20`.

[90] A. W. Harrow, A. Hassidim, and S. Lloyd. Quantum algorithm for linear systems of equations. *Phys. Rev. Lett.*, 103:150502, Oct 2009. doi: 10.1103/PhysRevLett.103.150502. URL `https://link.aps.org/doi/10.1103/PhysRevLett.103.150502`.

[91] A. Engel, G. Smith, and S. E. Parker. Quantum algorithm for the vlasov equation. *Phys. Rev. A*, 100:062315, 2019. doi: 10.1103/PhysRevA.100.062315.

[92] G. H. Low and I. L. Chuang. Hamiltonian Simulation by Qubitization. *Quantum*, 3:163, July 2019. ISSN 2521-327X. doi: 10.22331/q-2019-07-12-163. URL `https://doi.org/10.22331/q-2019-07-12-163`.

[93] K. Kubo, Y. O. Nakagawa, S. Endo, and S. Nagayama. Variational quantum simulations of stochastic differential equations. *Phys. Rev. A*, 103:052425, May 2021. doi: 10.1103/PhysRevA.103.052425. URL `https://link.aps.org/doi/10.1103/PhysRevA.103.052425`.

[94] I. V. Sokolov, N. M. Naumova, J. A. Nees, and G. A. Mourou. Pair creation in qed-strong pulsed laser fields interacting with electron beams. *Phys. Rev. Lett.*, 105:195005, Nov 2010. doi: 10.1103/PhysRevLett.105.195005. URL `https://link.aps.org/doi/10.1103/PhysRevLett.105.195005`.

[95] F. Del Gaudio, T. Grismayer, R. A. Fonseca, and L. O. Silva. Compton scattering in particle-in-cell codes. *Journal of Plasma Physics*, 86(5):905860516, 2020. doi: 10.1017/S002237782000118X.

[96] G. E. F. Oliveira. Statistical mechanics of the kompaneets equation, 2021. URL `https://arxiv.org/abs/2107.07549`.

[97] A. Peruzzo, J. McClean, P. Shadbolt, M.-H. Yung, X.-Q. Zhou, P. J. Love, A. Aspuru-Guzik, and J. L. O'Brien. A variational eigenvalue solver on a photonic quantum processor. *Nature Communications*, 5(1):4213, Jul 2014. ISSN 2041-1723. doi: 10.1038/ncomms5213. URL `https://doi.org/10.1038/ncomms5213`.

[98] L. Cincio, Y. Subaşı, A. T. Sornborger, and P. J. Coles. Learning the quantum algorithm for state overlap. *New Journal of Physics*, 20(11):113022, nov 2018. doi: 10.1088/1367-2630/aae94a. URL `https://doi.org/10.1088/1367-2630/aae94a`.

[99] Ibm quantum. URL:`https://quantum-computing.ibm.com/`.

[100] Y. Shi, A. R. Castelli, X. Wu, I. Joseph, V. Geyko, F. R. Graziani, S. B. Libby, J. B. Parker, Y. J. Rosen, L. A. Martinez, and J. L. DuBois. Quantum computation of three-wave interactions with engineered cubic couplings, 2020. URL `https://arxiv.org/abs/2004.06885`.

[101] S. Sim, P. D. Johnson, and A. Aspuru-Guzik. Expressibility and entangling capability of parameterized quantum circuits for hybrid quantum-classical algorithms. *Advanced Quantum Technologies*, 2(12):1900070, 2019. doi: https://doi.org/10.1002/qute.201900070. URL `https://onlinelibrary.wiley.com/doi/abs/10.1002/qute.201900070`.

[102] D. G. Green and C. N. Harvey. Transverse spreading of electrons in high-intensity laser fields. *Phys. Rev. Lett.*, 112:164801, Apr 2014. doi: 10.1103/PhysRevLett.112.164801.

[103] W. Yan, C. Fruhling, G. Golovin, D. Haden, J. Luo, P. Zhang, B. Zhao, J. Zhang, C. Liu, M. Chen, S. Chen, S. Banerjee, and D. Umstadter. High-order multiphoton thomson scattering. *Nature Photonics*, 11(8):514–520, Aug 2017. ISSN 1749-4893. doi: 10.1038/nphoton.2017.100.

[104] F. Mackenroth, A. R. Holkundkar, and H.-P. Schlenvoigt. Ultra-intense laser pulse characterization using ponderomotive electron scattering. *New Journal of Physics*, 21(12):123028, dec 2019. doi: 10.1088/1367-2630/ab5c4d.

[105] G. Hu, W.-Q. Sun, B.-J. Li, Y.-F. Li, W.-M. Wang, M. Zhu, H.-S. Hu, and Y.-T. Li. Quantum-stochasticity-induced asymmetry in the angular distribution of electrons in a quasiclassical regime. *Phys. Rev. A*, 102:042218, Oct 2020. doi: 10.1103/PhysRevA.102.042218.